



City Research Online

City, University of London Institutional Repository

Citation: Georgantzia, E., Gkantou, M., Kamaris, G. S. & Kansara, K. D. (2022). Design of aluminium alloy channel sections under minor axis bending. *Thin-Walled Structures*, 174, 109098. doi: 10.1016/j.tws.2022.109098

This is the published version of the paper.

This version of the publication may differ from the final published version.

Permanent repository link: <https://openaccess.city.ac.uk/id/eprint/34167/>

Link to published version: <https://doi.org/10.1016/j.tws.2022.109098>

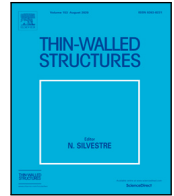
Copyright: City Research Online aims to make research outputs of City, University of London available to a wider audience. Copyright and Moral Rights remain with the author(s) and/or copyright holders. URLs from City Research Online may be freely distributed and linked to.

Reuse: Copies of full items can be used for personal research or study, educational, or not-for-profit purposes without prior permission or charge. Provided that the authors, title and full bibliographic details are credited, a hyperlink and/or URL is given for the original metadata page and the content is not changed in any way.

City Research Online:

<http://openaccess.city.ac.uk/>

publications@city.ac.uk



Full length article

Design of aluminium alloy channel sections under minor axis bending

Evangelia Georgantzia*, Michaela Gkantou, George S. Kamaris, Kunal D. Kansara

School of Civil Engineering and Built Environment, Liverpool John Moores University, L3 3AF Liverpool, United Kingdom



ARTICLE INFO

Keywords:

Aluminium alloys
Beam tests
Channel sections
Numerical modelling
Design standards
Plastic effective width

ABSTRACT

In recent years, numerous research works have been reported on the flexural response of aluminium alloy tubular cross-sections. However, studies on monosymmetric cross-sections and particularly channel (C-) sections are limited, albeit their increased usage in structural applications. This paper aims to address this knowledge gap providing an improved understanding about the minor axis bending behaviour of C-sections through an experimental and numerical investigation. In total 14 specimens made from 6082-T6 heat-treated aluminium alloy were subjected to four-point bending. Tensile coupon tests were also performed to determine the mechanical properties of the examined aluminium alloy. The obtained experimental results are analysed and discussed. A series of geometrically and materially nonlinear analyses were also carried out to study the flexural performance of C-sections in two aluminium alloys and two bending orientations over a range of cross-sectional aspect ratios and slendernesses. The experimental and numerical results are utilised to assess the European design standards. The applicability of the Continuous Strength Method and the Direct Strength Method is also evaluated. An alternative design method based on the plastic effective width concept is proposed for slender C-sections subjected to minor axis bending. This method accounts for the inelastic reserve capacity which is in accordance with the experimental and numerical observations.

1. Introduction

Nowadays, aluminium alloys are increasingly employed as structural material in the construction industry. For example, aluminium alloys were used to support the glazing system of the Sage Gateshead building in Gateshead, United Kingdom and to form the modular façade elements of the Casablanca Finance City Tower in Casablanca, Morocco. 6000 series aluminium alloys, known as structural alloys, are a great structural material choice, as they are able to satisfy strength requirements without increasing structure's self-weight. The fact that they reflect the ultraviolet radiation and are resistant against corrosion provides a longer service life and reduces the maintenance cost of the structure. These characteristics together with their high recyclability demonstrate their strong potential as a structural material.

Over the last 20 years, several experimental and numerical investigations have been reported on the flexural response of aluminium alloy cross-sections considering various geometrical shapes [1]. Opheim [2] performed four-point bending tests on square hollow sections (SHSs) and found that the flexural strength is highly dependent on the parameters involved in the material stress-strain relationship. Moen et al. [3,4] conducted tests and finite element (FE) studies on SHSs, unwelded and welded I-sections concluding the beneficial influence of material strain hardening on the rotational capacity. Their reported test data were utilised by De Matties et al. [5] to propose new cross-section

classification limits for EN 1999-1-1 [6] accounting for material strain hardening. The significance of the material strain hardening on the cross-sectional response was also pointed out a few years later in a series of research studies carried out by Su et al. [7–10]. On the basis of experimental evidence, Zhu and Young [11] suggested modified design formulae of the current Direct Strength Method (DSM). Furthermore, Kim and Peköz [12] tested doubly symmetric I-sections and proposed a new design formula for the stress at ultimate limit state. Castaldo et al. [13] and Piluso et al. [14] suggested multivariate non-linear equations to determine the flexural resistance and rotational capacity of rectangular hollow section (RHS), I- and H-section beams. Moreover, a series of reported studies on circular hollow sections (CHSs) with and without perforations subjected to bending are available in [15–17].

It is obvious from the aforementioned literature that past research has mainly focused on the flexural performance of aluminium alloy tubular and doubly-symmetric open cross-sections, while research studies on monosymmetric aluminium alloy cross-sections and particularly channel (C-) sections are rather limited, despite their applicability in structures. C-sections as open sections are easy to connect during the assemblage and are often employed as rafters on light-duty roofs, studs in framed buildings, girts and pillars in curtain wall systems. Zhu et al. [18] tested plain and lipped C-sections under four-point bending and the obtained data were utilised to modify the current DSM improving its suitability for aluminium alloy flexural members.

* Corresponding author.

E-mail address: E.Georgantzia@2019.ljmu.ac.uk (E. Georgantzia).

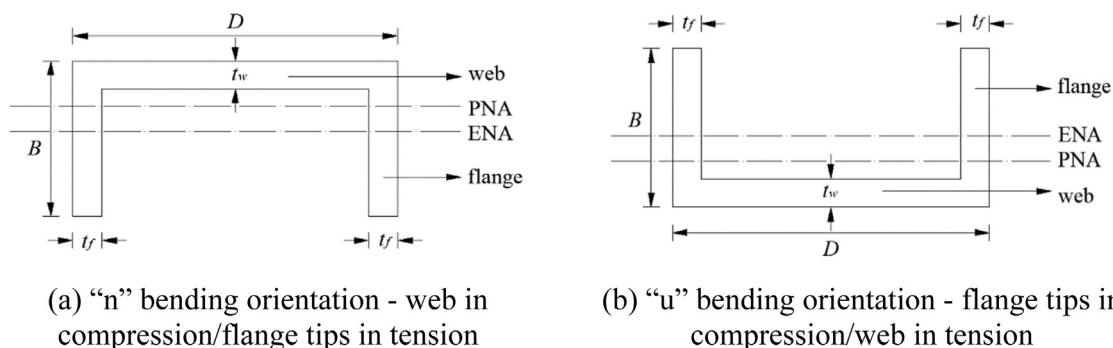


Fig. 1. Adopted notation for C-sections.

Table 1

Mean measured dimensions of the C-section beam specimens.

Specimen	orientation	D (mm)	B (mm)	t_w (mm)	t_f (mm)	L (mm)	ω_0 (mm)
50.8 × 50.8 × 6.35 – n	compression in web	50.92	50.84	6.34	6.29	1000.20	0.18 ($t_f/34$)
50.8 × 50.8 × 6.35 – u	compression in flange tips	51.07	50.78	6.36	6.27	1000.20	0.18 ($t_f/35$)
50.8 × 50.8 × 4.76 – n	compression in web	50.89	50.56	4.73	4.77	1000.80	0.30 ($t_f/16$)
50.8 × 50.8 × 4.76 – u	compression in flange tips	50.88	50.62	4.73	4.77	1000.90	0.32 ($t_f/15$)
76.2 × 76.2 × 6.35 – n	compression in web	76.28	76.26	6.33	6.24	1000.80	0.32 ($t_f/20$)
76.2 × 76.2 × 6.35 – u	compression in flange tips	76.44	76.28	6.27	6.27	1000.80	0.27 ($t_f/23$)
50.8 × 38.1 × 6.35 – n	compression in web	50.89	38.13	6.34	6.36	1001.00	0.35 ($t_f/18$)
50.8 × 38.1 × 6.35 – u	compression in flange tips	50.88	38.03	6.33	6.28	1001.00	0.35 ($t_f/18$)
50.8 × 38.1 × 3.18 – n	compression in web	50.81	37.95	3.15	3.11	1000.50	0.22 ($t_f/14$)
50.8 × 38.1 × 3.18 – u	compression in flange tips	50.77	37.95	3.13	3.15	1000.80	0.23 ($t_f/14$)
50.8 × 25.4 × 3.18 – n	compression in web	50.68	25.43	3.11	3.11	1001.00	0.24 ($t_f/13$)
50.8 × 25.4 × 3.18 – u	compression in flange tips	50.71	25.31	3.21	3.17	1001.00	0.21 ($t_f/15$)
38.1 × 38.1 × 4.76 – n	compression in web	37.97	37.97	4.64	4.64	1000.90	0.22 ($t_f/21$)
38.1 × 38.1 × 4.76 – u	compression in flange tips	37.98	37.93	4.71	4.60	1001.00	0.16 ($t_f/29$)

Pham et al. [19] investigated the global buckling response of simply-supported cold-rolled aluminium alloy C-section beams and developed new design formulae for the prediction of their global and distortional buckling capacity.

Aluminium alloys exhibit a rounded stress–strain behaviour and the influence of the nonlinear material response on the flexural capacity of monosymmetric cross-sections is not yet clarified. To address this knowledge gap, a comprehensive experimental programme was carried out to investigate the flexural performance of aluminium alloy C-sections and the obtained results are discussed in Section 2. In parallel, an extensive numerical parametric study was conducted to generate flexural performance data over a broad range of key parameters, as discussed in Section 3. The experimental and FE results are utilised in Section 4 to assess the European design standards [6]. The applicability of the Continuous Strength Method (CSM) [20] and the Direct Strength Method (DSM) [21] is also evaluated. An alternative design method based on the plastic effective width concept is proposed for slender C-sections subjected to minor axis bending. Conclusions are finally summarised in Section 5.

2. Experimental programme

The experimental investigation was performed in Light Structures and Materials Laboratory of the School of Civil Engineering and Built Environment at Liverpool John Moores University. A series of four-point bending tests was conducted to examine the flexural response of aluminium alloy C-section beams.

2.1. Test specimens and geometric imperfection measurements

A total of 7 C-sections with various geometrical dimensions were considered in the present study. The geometrical dimensions of the investigated cross-sections were selected so that to cover a wide variety of plate slendernesses ranging from 1.92–8.4 (see Table 3). These values enabled to examine the minor axis bending behaviour of C-sections

across the four cross-sectional Classes (Classes 1–4) specified in EN 1999–1–1 [6]. Each cross-section was tested in both the “n”, i.e., maximum compressive stresses in web/maximum tensile stresses in flange tips (see Fig. 1(a)), and the “u”, i.e., maximum compressive stresses in flange tips/maximum tensile stresses in web (see Fig. 1(b)), bending orientations. Prior to testing, the dimensions of the beam specimens were measured carefully and are set out in Table 1, where D is the outer web depth, B is the outer flange width, t_w is the web thickness, t_f is the flange thickness and L is the total specimen’s length. The adopted notation is also shown in Fig. 1, where the elastic (ENA) and plastic (PNA) neutral axes are also depicted. The specimens’ designation was defined according to the nominal geometric dimensions ($D - B - (t_w + t_f)/2$) followed by the letter “u” or “n” which signifies the bending orientation.

The geometric imperfections owing to the manufacturing process of thin-walled structural members may significantly affect their strength, precipitating the occurrence of local buckling. Since the present study deals with minor axis bending and the flanges are under stress gradient, lateral–torsional buckling is precluded and thereby only the local geometric imperfections were measured. Aiming to obtain a representative geometric imperfection pattern, each specimen was secured to a flat surface table and a ball probe attached onto the scribing jaw was moving along a line inscribed over the full specimen length. Measurements were taken using a Mitutoyo linear height gauge at 20 mm intervals. For each measuring point, the maximum deviation from a datum plane was assumed as local imperfection amplitude. The maximum measured local imperfection amplitude ω_0 for each beam specimen is taken as the maximum value of the measured local imperfection amplitudes of both flanges and web and is listed in Table 1.

2.2. Aluminium 6082-T6: tensile coupon tests

Material tensile tests were also performed on flat coupons to determine the mechanical properties of the 6082-T6 heat-treated aluminium alloy. For each examined cross-section, flat coupons were extracted and

Table 2
Material properties obtained from tensile coupon tests.

Specimen	E (MPa)	$\sigma_{0.1}$ (MPa)	$\sigma_{0.2}$ (MPa)	σ_u (MPa)	ϵ_u (%)	ϵ_f (%)	n	$\sigma_u/\sigma_{0.2}$
50.8 × 50.8 × 6.35	66729	275	282	324	7.5	13.5	27.6	1.15
50.8 × 50.8 × 4.76	69302	284	292	332	9.1	12.9	25.0	1.14
76.2 × 76.2 × 6.35	70885	280	286	317	8.8	16.2	32.7	1.11
50.8 × 38.1 × 6.35	67009	290	298	334	7.5	12.7	25.5	1.12
50.8 × 38.1 × 3.18	67500	280	287	316	8.2	13.2	28.1	1.10
50.8 × 25.4 × 3.18	66408	276	282	295	6.3	11.4	32.2	1.05
38.1 × 38.1 × 4.76	68744	290	297	309	6.5	13.0	29.1	1.04

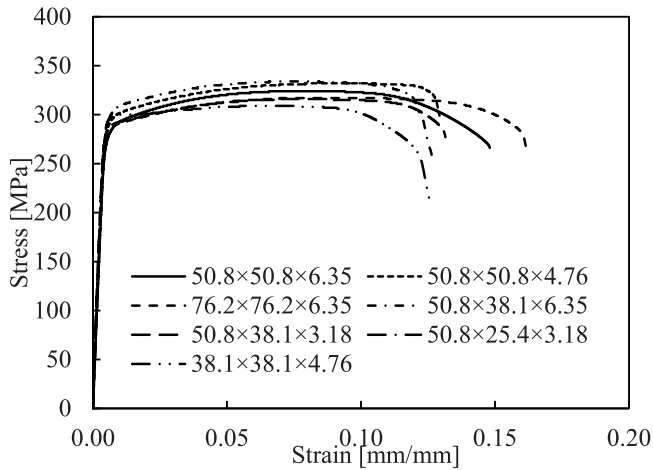


Fig. 2. Experimental stress–strain curves.

machined in line with the geometric requirements described in EN ISO 6892-1 [22]. The geometry for all coupons is shown in Fig. 3(a). The coupons were subjected to tensile loading in a 50 kN Tinius Olsen machine with a displacement rate of 0.2 mm/min. An extensometer was mounted onto the central necked part of the coupon to record the longitudinal strains during testing. The average measured material properties, including the initial modulus of elasticity E , the 0.1% proof stress $\sigma_{0.1}$, the 0.2% proof stress $\sigma_{0.2}$, the ultimate tensile stress σ_u , the strain corresponding to ultimate tensile stress ϵ_u , the strain at fracture ϵ_f and the strain hardening exponent n [23,24] are summarised in Table 2.

Fig. 2 shows the experimental stress–strain ($\sigma - \epsilon$) curves, showing a rounded nonlinear stress–strain behaviour with continuous strain hardening. The strain hardening ratio $\sigma_u/\sigma_{0.2}$ for each examined cross-section is also listed in Table 2, reaching up to 115%. The curves do not exhibit a distinct yield point and thus the onset of yielding is considered at 0.2% strain. Figs. 3(a) and 3(b) depict typical coupon specimens during and after tensile testing, respectively. Note that the obtained test data were utilised in the subsequent numerical study in Section 3.

2.3. Four-point bending tests

A series of 14 tests was performed aiming to investigate the minor axis flexural response of aluminium alloy C-sections. Figs. 4 and 5 illustrate a schematic diagram and a photograph of the four-point test setup, respectively. The specimens are simply-supported beams and thus steel rollers were used to form their boundary conditions allowing the rotation around the minor axis and displacement along the longitudinal axis of the specimens. The specimens had a clear span equal to 900 mm and a 50 mm overhang from both sides. The span-to-height ratio was over 10 [25,26] to ensure that the cross-sectional flexural capacity will be attained without any shear effects. In line with past studies [26], underpinning bolts were inserted between the flanges and G-clamps were located onto the outer faces of the flanges at the loading points and supports, to prevent web crippling occurrence.

The four-point bending tests were performed using a Mayes servo-controlled hydraulic testing machine with 600 kN maximum capacity. The load of the machine was applied at a cross-head displacement rate of 0.8 mm/min and introduced as two loads at third points in the specimens through a steel beam (Fig. 4). 100 mm × 70 mm × 10 mm steel plates were, also, welded to the steel rollers to spread uniformly the applied load.

In order to determine the specimens' curvature at the constant moment area, three linear variable displacement transducers (LVDTs) were located at the mid-span and the two loading points to capture the vertical deflections. The position of the neutral axis (NA) during testing was monitored through three linear electrical resistance strain gauges attached at the mid-span. Particularly, two strain gauges were affixed at both flanges at 10 mm from the tip and the third one at the middle of the web, as shown in Fig. 4. The applied loading was measured using the load cell of the machine. The applied loading, vertical deflection and strain values were recorded through a data acquisition equipment with sampling frequency of 10 Hz.

Table 3 reports the key test results, including the ultimate experimental bending moment $M_{u,Exp}$ and the calculated elastic M_{el} and plastic M_{pl} cross-sectional bending moment resistances. To facilitate the comparison, the moment–curvature responses derived from tests are plotted in a non-dimensional format, as shown in Fig. 6; the moment in the mid-span is normalised by the plastic moment resistance M_{pl} , which is taken by multiplying the 0.2% proof (yield) stress acquired from the tensile coupon tests by the plastic section modulus about the minor axis (also shown in Fig. 1). The curvature κ in the constant moment area of the beam, i.e. between the loading points, can be determined by Eq. (1) assuming that the deformed shape of the central span (of length L_2) represents a segment of a circular arc (of radius r) [27].

$$\kappa = \frac{1}{r} = \frac{8(\delta_M - \delta_L)}{4(\delta_M - \delta_L)^2 + L_2^2} \quad (1)$$

where δ_M is the reading taken from the LVDT placed at the mid-span whilst δ_L is the average reading taken from the LVDTs placed at the two loading points. The curvature κ at the constant moment area is normalised by κ_{pl} which is the elastic component of the curvature corresponding to M_{pl} , as expressed in Eq. (2).

$$\kappa_{pl} = \frac{M_{pl}}{EI} \quad (2)$$

where E is the modulus of elasticity determined from the tensile coupon tests (Table 2) and I is the second moment of area of the cross-section about the minor axis. The experimentally obtained normalised curvature $\kappa_{u,Exp}/\kappa_{pl}$ for each tested beam is also listed in Table 3.

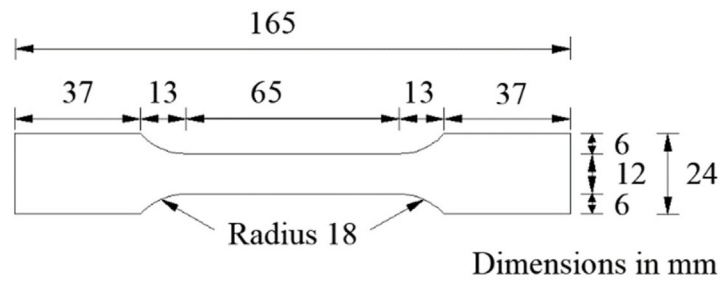
Table 3 also provides the cross-sections' Class according to EN 1999-1-1 [6] and the corresponding slenderness ratios β_w/ϵ and β_f/ϵ for internal web in compression and outstand flange in bending, respectively. In the slenderness ratios expressions, $\beta_w = d/t_w$ and $\beta_f = 0.7b/t_f$, are the slenderness parameters (d is the compressed flat web width and b is the flat flange width) and $\epsilon = \sqrt{250/\sigma_{0.2}}$ is the material coefficient.

It is noteworthy that the difference in response of the specimen 50.8×50.8×6.35 (Fig. 6(a)) under the two different bending orientations can be attributed to the fact that it is classified as Class 2 in “n” bending orientation and as Class 3 in “u” orientation, hence reaching larger normalised moment in the first case.

Table 3
Summary of key results obtained from the four-point bending tests.

Specimen	Internal web in compression		Outstand flange in bending		M_{el} (kNm)	M_{pl} (kNm)	M_{pl} / M_{el}	$M_{u,Exp}$ (kNm)	$M_{u,Exp} / M_{el}$	$M_{u,Exp} / M_{pl}$	$\kappa_{u,Exp} / \kappa_{pl}$	Failure mode
	β_w / ϵ	Class	β_f / ϵ	Class								
50.8 × 50.8 × 6.35 – n	2.11	1	4.3	2	2.03	3.49	1.73	5.56	2.74	1.59	13.30	yielding
50.8 × 50.8 × 6.35 – u	- ^a	- ^a	5.2	3	2.02	3.49	1.73	3.91	1.93	1.12	8.39	local buckling
50.8 × 50.8 × 4.76 – n	3.26	1	6.3	4	1.58	2.76	1.74	3.36	2.12	1.22	7.80	yielding
50.8 × 50.8 × 4.76 – u	- ^a	- ^a	7.3	4	1.50	2.64	1.75	2.90	1.93	1.10	4.30	local buckling
76.2 × 76.2 × 6.35 – n	2.38	1	4.6	3	4.48	7.86	1.76	10.30	2.30	1.31	24.00	yielding
76.2 × 76.2 × 6.35 – u	- ^a	- ^a	8.4	4	4.20	7.45	1.77	8.19	1.95	1.10	5.60	local buckling
50.8 × 38.1 × 6.35 – n	1.92	1	2.8	1	1.23	2.18	1.78	2.83	2.10	1.30	11.40	yielding
50.8 × 38.1 × 6.35 – u	- ^a	- ^a	3.8	2	1.21	2.16	1.78	2.75	2.19	1.17	7.15	local buckling
50.8 × 38.1 × 3.18 – n	5.28	1	7.2	4	0.58	1.05	1.81	1.35	2.31	1.28	6.41	yielding
50.8 × 38.1 × 3.18 – u	- ^a	- ^a	8.3	4	0.55	1.00	1.81	1.12	2.03	1.12	2.79	local buckling
50.8 × 25.4 × 3.18 – n	4.65	1	4.5	3	0.28	0.51	1.80	0.59	2.11	1.17	7.60	yielding
50.8 × 25.4 × 3.18 – u	- ^a	- ^a	5.2	3	0.28	0.51	1.80	0.56	1.98	1.10	5.66	local buckling
38.1 × 38.1 × 4.76 – n	2.23	1	4.6	3	0.87	1.51	1.73	1.69	1.93	1.12	7.15	yielding
38.1 × 38.1 × 4.76 – u	- ^a	- ^a	5.5	3	0.88	1.51	1.73	1.63	1.86	1.08	5.50	local buckling

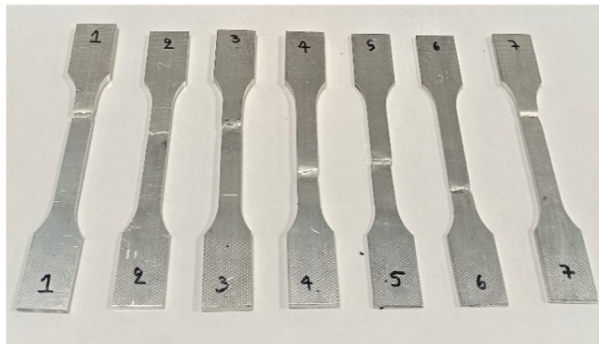
^aInternal web is tension in the “u” bending orientation.



(a) Geometry



(a) During testing



(b) After testing

Fig. 3. Tensile coupon specimens.

Material yielding (Fig. 7(a)) and local buckling (Fig. 7(b)) were the governing failure modes for beam specimens under “n” and “u” bending orientation, respectively. All failed specimens are displayed in

Fig. 8. Specimens’ labelling is, also, depicted followed by the resulting failure mode denoted by letters “Y” or “LB” for material yielding and local buckling, respectively. As can be seen from Fig. 6, most specimens

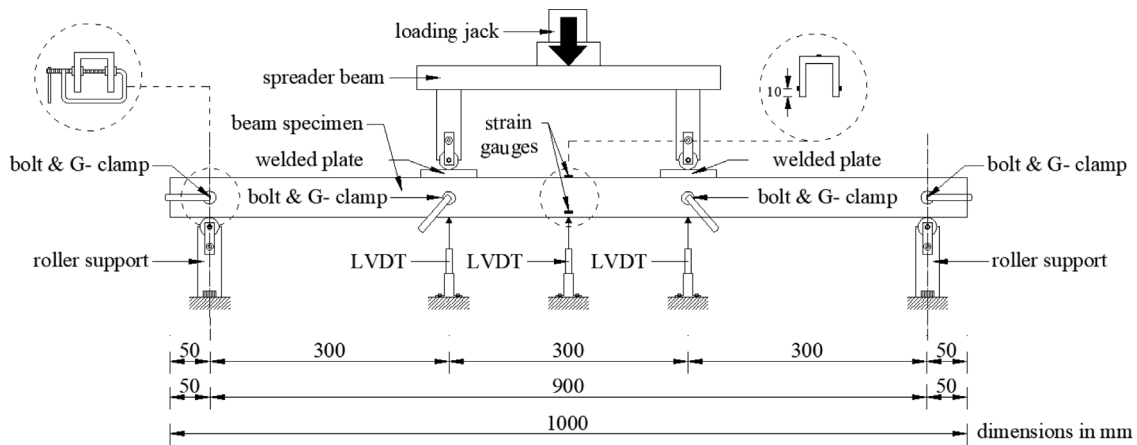


Fig. 4. Schematic illustration of the four-point bending test setup.

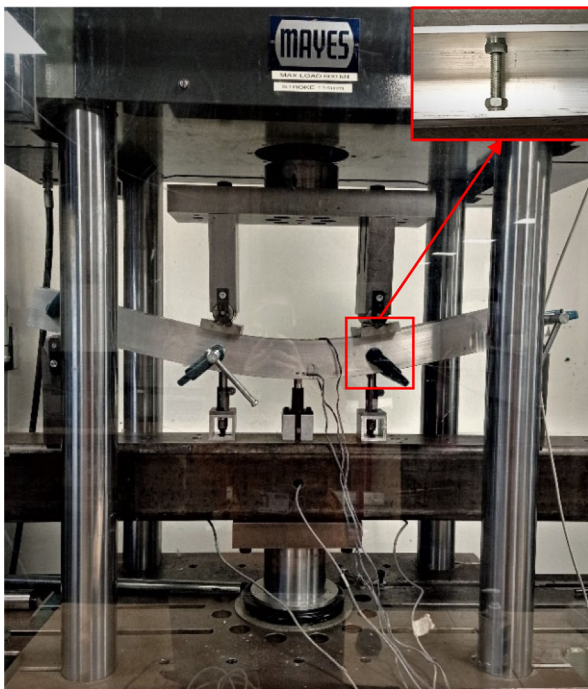


Fig. 5. Typical four-point bending test setup.

bent in the “u” orientation failed in lower curvature values compared to their counterparts bent in the “n” orientation. This observation demonstrates the fact that a C-section is more susceptible to local buckling when the maximum compressive stresses are induced in the flange tips, i.e., “u” orientation, rather than in the web, i.e., “n” orientation. The same was also concluded in similar past studies conducted on stainless and high strength steel C-sections [25,28]. Moreover, the quite steep softening branch of the curves of the 50.8×50.8×4.76-u, 76.2×76.2×6.35-u and 50.8×38.1×3.18-u specimens indicates a brittle post-ultimate behaviour, i.e., low capability for inelastic deformations with significant loss of strength. This was anticipated since these beam specimens comprised slender sections.

3. Numerical study

A parallel numerical study was carried out in the commercial software package ABAQUS [29] to extend the pool of flexural performance data for aluminium alloy C-sections. This section discusses the modelling assumptions, the model validation and the parametric study.

3.1. Modelling methodology and assumptions

The four-node shell element with reduced integration rule (S4R) and three translational and three rotational degrees of freedom was adopted to discretise the developed FE models. Its mathematical formula considers arbitrarily large rotations and finite membrane strains and thereby is suitable for materially and geometrically nonlinear analyses. The S4R shell element was also employed in similar past studies [18,19,28,30–36] capturing accurately the flexural response of C-sections. Aiming to minimise the computational time without compromising the accuracy of the results, a mesh convergence study was conducted resulting in a uniform mesh with a size equal to 5 mm × 5 mm. Despite the symmetry in loading, boundary conditions and geometry with respect to the plane of bending, the length and the cross-section of the examined beam specimens were modelled assigning their full geometrical dimensions to also consider possible antisymmetric local buckling modes [37]. The support and loading conditions were defined by restraining suitable degrees of freedom according to the experimental setup, as shown in Fig. 9. To consider the stiffening effect provided by the underpinning bolts and the G-clamps, distributing coupling constraints were assigned to ensure that the cross-sections at the respective locations remained undeformed during the analysis.

An elastic–plastic material model with a von Mises yield criterion and isotropic hardening rule was employed to simulate the mechanical response of the investigated aluminium alloy. Following the ABAQUS [29] requirement for material modelling, the engineering (nominal) stress σ_{nom} and strain ϵ_{nom} values obtained from the tensile coupon tests were converted to true stress $\sigma_{true} = \sigma_{nom}(1 + \epsilon_{nom})$ and true plastic strain $\epsilon_{true}^{pl} = \ln(1 + \epsilon_{nom}) - \frac{\sigma_{nom}}{E}$ values.

Initial geometric imperfections should be incorporated into the FE models [7,36,38,39]. For each modelled beam specimen, a linear eigenvalue buckling analysis was carried out and the lowest elastic buckling mode shape in accordance with the experimentally obtained failure mode was superposed into a following geometrically and materially nonlinear analysis. An amplitude equal to the average measured local imperfection amplitude was adopted. Regarding the nonlinear analysis, the modified Riks solution method was employed to trace the full moment–curvature response of the developed FE models.

The residual stresses resulting from the heat-treatment process of the aluminium alloys [40–42], are expected to have insignificant influence on the ultimate resistance of extruded aluminium alloy cross-sections and were not explicitly included in the numerical modelling herein [43,44].

3.2. Validation of the FE models

Aiming to verify the accuracy level of the developed FE models, the numerically obtained moment–curvature responses, ultimate

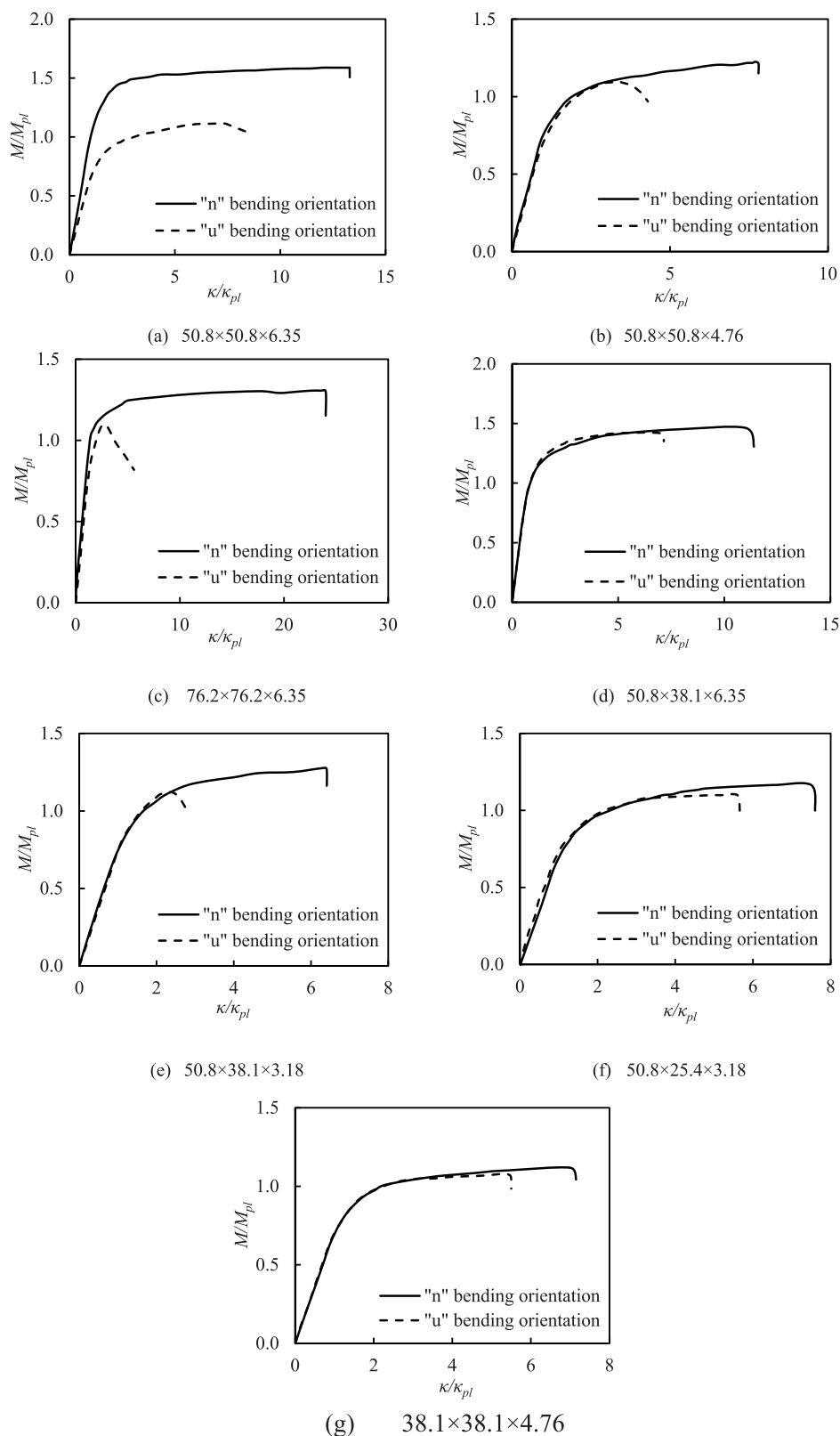


Fig. 6. Normalised moment versus curvature responses obtained from the four-point bending tests.

bending moment capacities ($M_{u,FE}$) and failure modes were compared with the corresponding experimental ones. The $M_{u,Exp}/M_{u,FE}$ ratios are reported in Table 4, achieving a mean value and corresponding coefficient of variation (COV) of 1.01 and 0.04, respectively,

thereby suggesting accurate and consistent numerical predictions. Typical moment–curvature responses are depicted in Fig. 10, showing that the developed FE models can capture well the experimental initial stiffness, ultimate bending moment capacity and inelastic response.

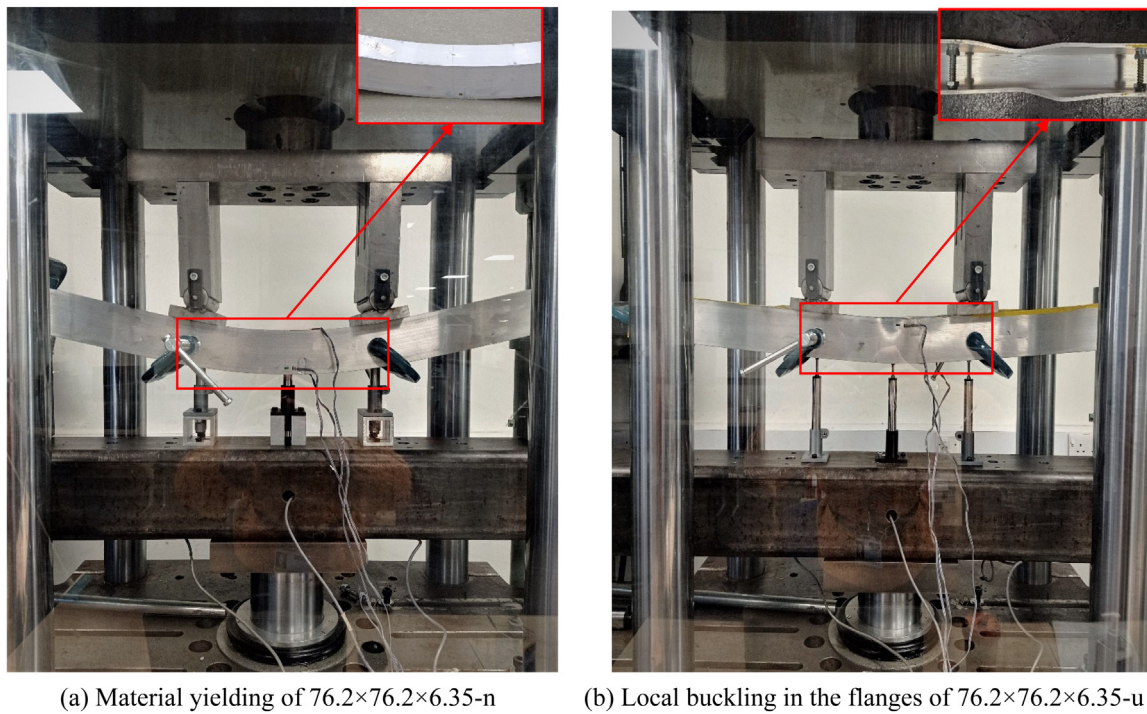


Fig. 7. Typical failure modes obtained from four-point bending tests.

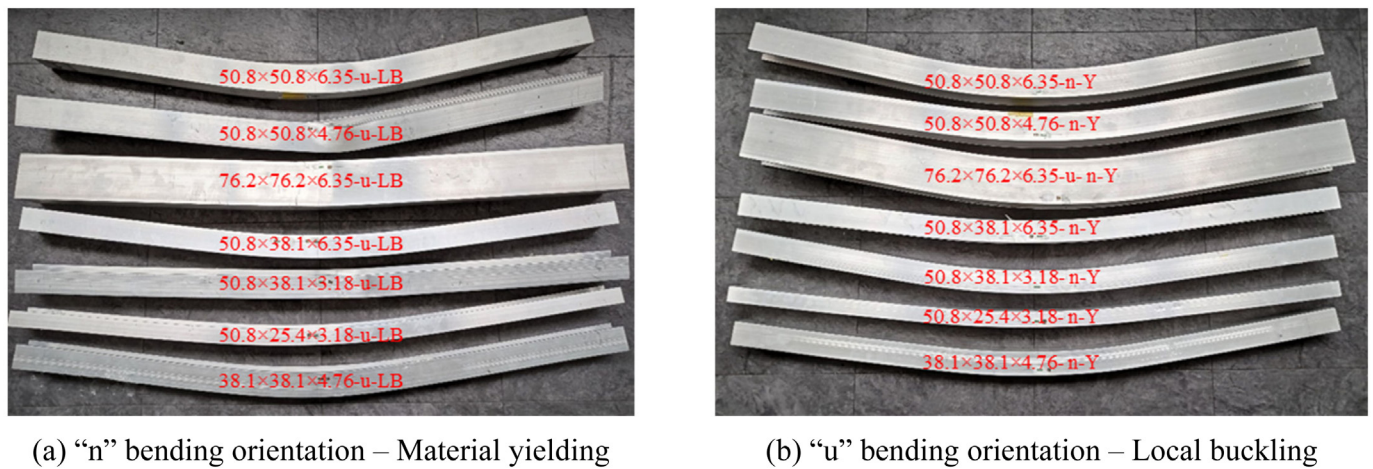


Fig. 8. Failure modes obtained from four-point bending tests.

Numerical failure modes also accurately capture the experimental ones, as shown in Fig. 11. Thus, it can be concluded that the developed FE models can successfully predict the flexural performance of aluminium alloy C-sections.

3.3. Parametric study

3.3.1. Outline

Having validated the developed FE models against the experimental results, a series of parametric studies was conducted to investigate the influence of key parameters on the flexural performance of C-sections. The examined parameters are summarised in Table 5. Three different aspect ratios D/B were considered, namely 1.0, 1.5 and 2.0, keeping the outer web depth D fixed to 100 mm. A total of twelve cross-sectional thicknesses ($t_w=t_f$) were examined, extending the experimental data to a broad range of plate slendernesses. Particularly, the slenderness ratio β_w/ϵ ranges from 3.44 to 51.34, whilst the slenderness ratio β_f/ϵ ranges from 1.20 to 24.21. Moreover, the cross-sectional slenderness

$\bar{\lambda}_{cs} = \sqrt{\sigma_{0.2}/\sigma_{cr}}$ ranges from 0.10 to 2.14. Aiming to extend the study to an additional structural aluminium alloy, two types of heat-treated aluminium alloys were investigated, namely 6082-T6 and 6063-T5, representing a typical high and normal strength heat-treated aluminium alloy, respectively. The average material properties obtained from the tensile coupon tests of this study were adopted for 6082-T6, whilst for 6063-T5 the material properties reported in [10] were adopted. The material properties of both examined aluminium alloys are summarised in Table 6. All specimens had a clear span $L = 900$ mm and were subjected to four-point bending with two equal loads at third points considering both the “u” and “n” orientation. Initial local geometric imperfections were accounted for through the lowest buckling mode shape with an amplitude equal to the average measured local imperfection amplitude. A total of 140 numerical analyses were executed and the obtained results are discussed in the following subsections.

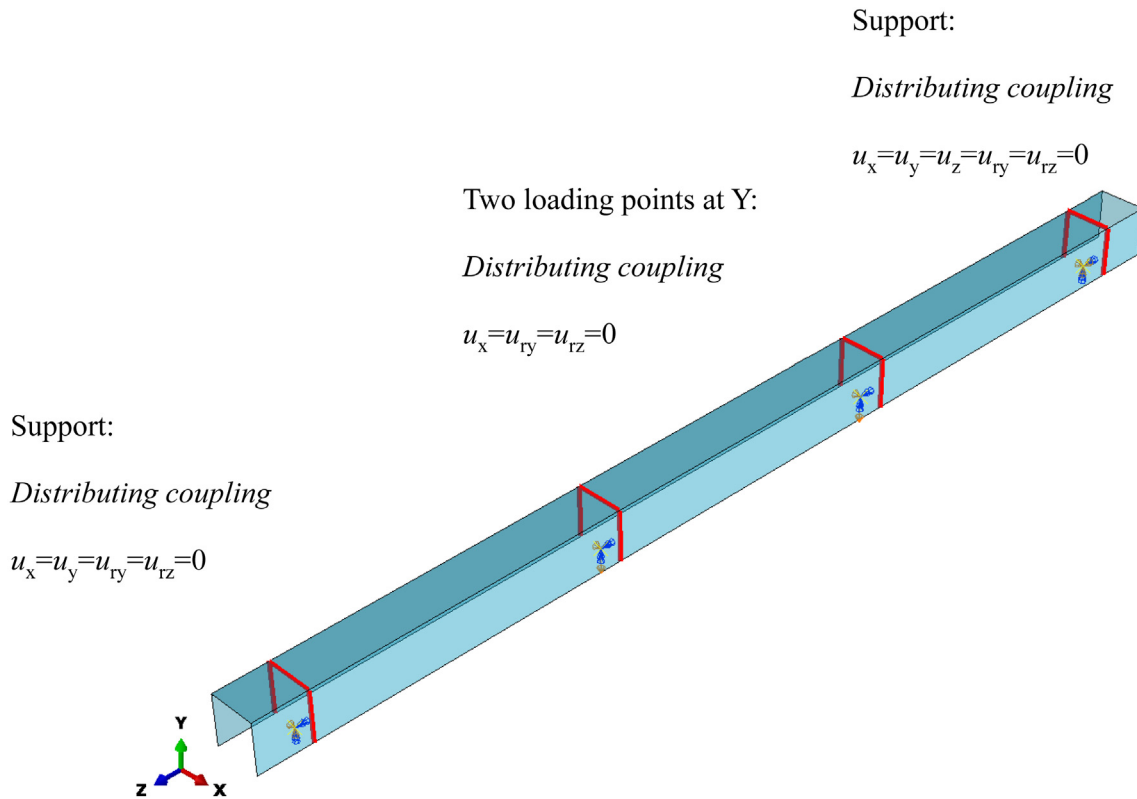


Fig. 9. Modelled geometry of a typical beam specimen and the corresponding applied boundary conditions.

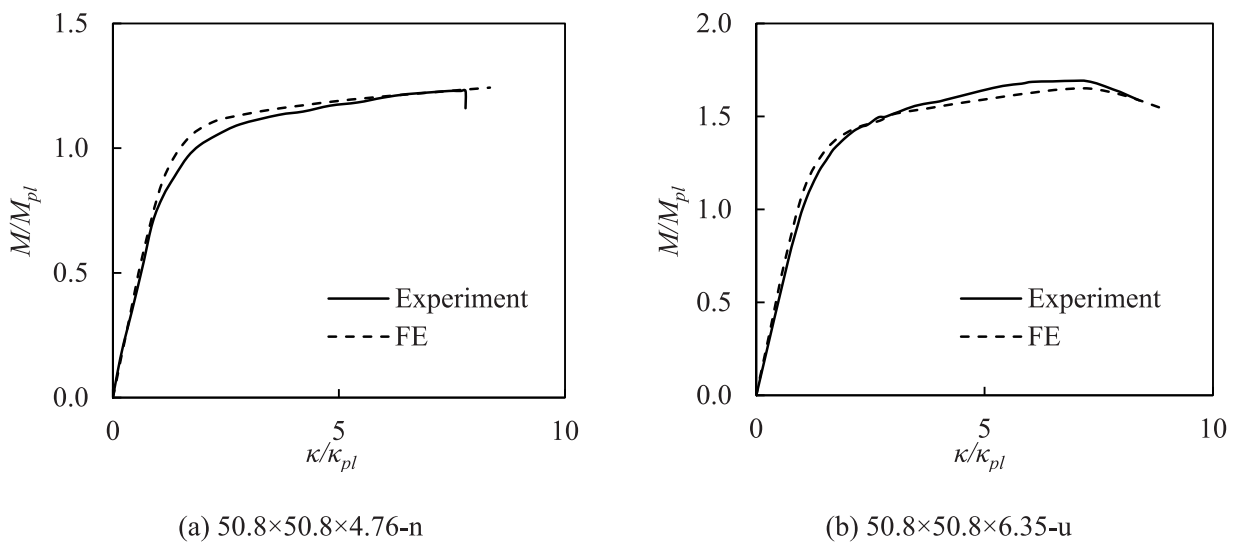


Fig. 10. Comparison between typical FE and experimental normalized moment–curvature curves.

3.3.2. Influence of cross-sectional aspect ratio, slenderness and aluminium alloy type

For all examined FE models, the exhibited moment–curvature response, the ultimate bending moment capacity and the failure mode were recorded. All C-sections under “u” bending orientation failed due to local buckling initiated in the compressed part of the flanges. For C-sections under “n” bending orientation, material yielding was the governing failure mode. To evaluate the generated results, the FE ultimate bending moments $M_{u,FE}$ were normalised by the corresponding plastic bending moment resistances M_{pl} and were plotted against the slenderness parameter β_w/ϵ and β_f/ϵ for the “n” and “u” bending orientation, respectively.

Fig. 12 depicts the results for the “n” bending orientation separately for the three different aspect ratios under consideration. It is evident that the 6063-T5 C-sections exhibit higher normalised bending moment capacities throughout the considered β_w/ϵ range, with the M_{pl} being exceeded by up to 30% compared to their 6082-T6 counterparts. This is related to the more favourable strain hardening properties of 6063-T5, i.e., lower strain hardening exponent n , which results in higher tangent stiffnesses in the inelastic range enabling for higher normalised bending moment capacities. Moreover, from Fig. 12 it can be concluded that the aspect ratio does not significantly influence the bending moment capacity as the governing failure mode was material yielding.

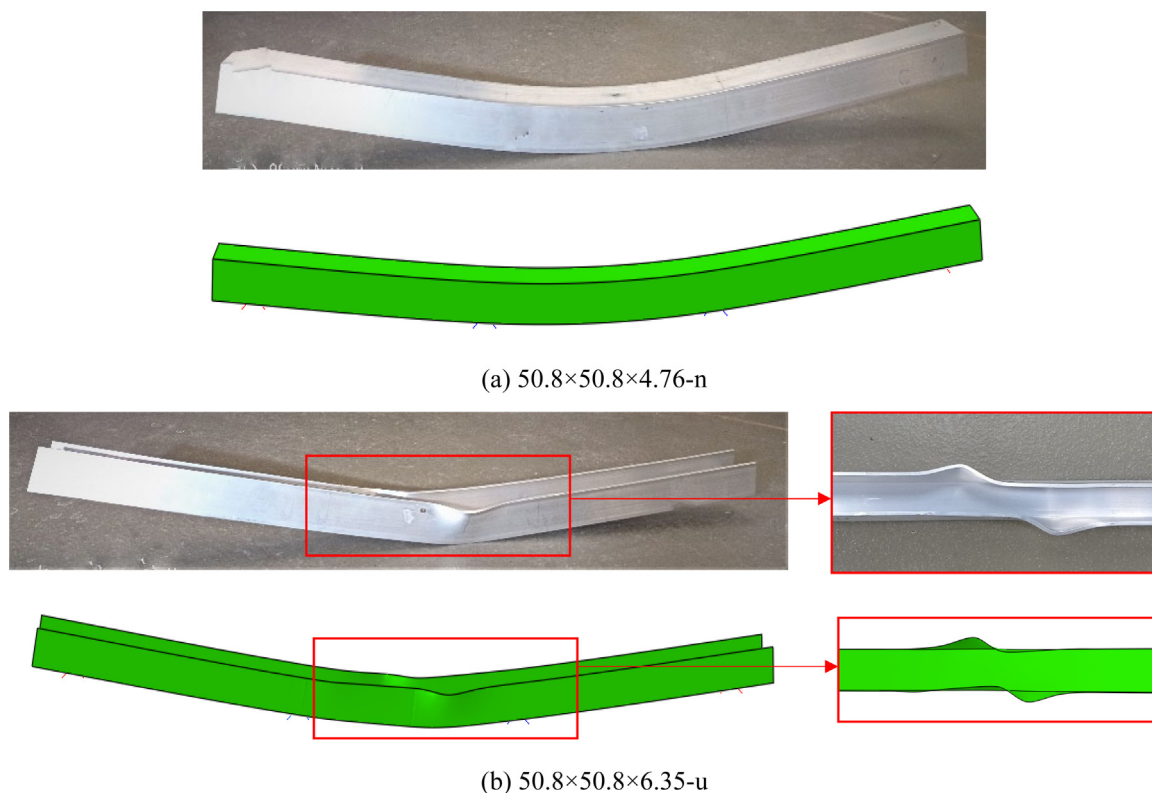


Fig. 11. Comparison between typical FE and experimental failure modes.

Table 4
Comparison between the FE and experimental bending moment capacities.

Specimen	$M_{u,Exp}/M_{u,FE}$
50.8 × 50.8 × 6.35 – n	0.95
50.8 × 50.8 × 6.35 – u	1.03
50.8 × 50.8 × 4.76 – n	1.00
50.8 × 50.8 × 4.76 – u	1.01
76.2 × 76.2 × 6.35 – n	0.98
76.2 × 76.2 × 6.35 – u	0.97
50.8 × 38.1 × 6.35 – n	1.02
50.8 × 38.1 × 6.35 – u	0.93
50.8 × 38.1 × 3.18 – n	1.05
50.8 × 38.1 × 3.18 – u	1.07
50.8 × 25.4 × 3.18 – n	1.06
50.8 × 25.4 × 3.18 – u	0.98
38.1 × 38.1 × 4.76 – n	1.05
38.1 × 38.1 × 4.76 – u	1.01
mean	1.01
COV	0.04

Table 5
List of key parameters considered in parametric studies.

	Total FE analyses: 140
2 aluminium alloys	<ul style="list-style-type: none"> • 6082-T6 • 6063-T5
3 aspect ratios D/B ($D \times B$) (mm × mm):	<ul style="list-style-type: none"> • 1.0 (100 × 100) • 1.5 (100 × 66.7) • 2.0 (100 × 50)
12 plate thicknesses $t_w=t_f$ (mm) Resulting slenderness	<ul style="list-style-type: none"> • 2, 3, 4, 5, 6, 7, 8, 9, 10, 12, 14, 16 • Resulting slenderness β_w/ϵ: 3.44-51.34 β_f/ϵ: 1.20-24.21 λ_{cs}: 0.10-2.14

Table 6
Material properties for 6082-T6 and 6063-T5 [10] aluminium alloys considered in parametric studies.

	E (MPa)	$\sigma_{0.2}$ (MPa)	σ_u (MPa)	n	ϵ_u (%)	ϵ_f (%)
6082-T6	70885	286	317	32.7	8.8	16.2
6063-T5	69000	164	211	10.0	7.3	13.7

Similarly, Fig. 13 shows the results for the “u” bending orientation. It can be seen that the stocky 6063-T5 C-sections exhibit higher normalised bending moment capacities, with the M_{pl} being exceeded by up to 60% compared to their 6082-T6 counterparts. Again, this is related to the more favourable strain hardening properties of 6063-T5. For more slender C-sections, the influence of the aluminium alloy type on the normalised flexural behaviour is minimal, as failure is triggered by local buckling before the attainment of the yield strength. Moreover, the normalised bending moment capacity of slender sections significantly improves with decreasing aspect ratios. This is attributed to the beneficial influence of the plate element interaction on the local buckling response of the compression flange of sections with lower aspect ratios (i.e., shorter webs provide greater resistance to local buckling of the flanges).

4. Assessment of international design codes and design methods

In this section the ultimate bending moment capacities obtained from the experiments and parametric studies are utilised to evaluate the applicability and accuracy of the design rules specified in Eurocode 9 (EC9) [6]. Three design approaches are also assessed; the CSM [20], the DSM [21] and the plastic effective width method [45]. It is noted that throughout the comparisons all partial safety factors were set equal to unity.

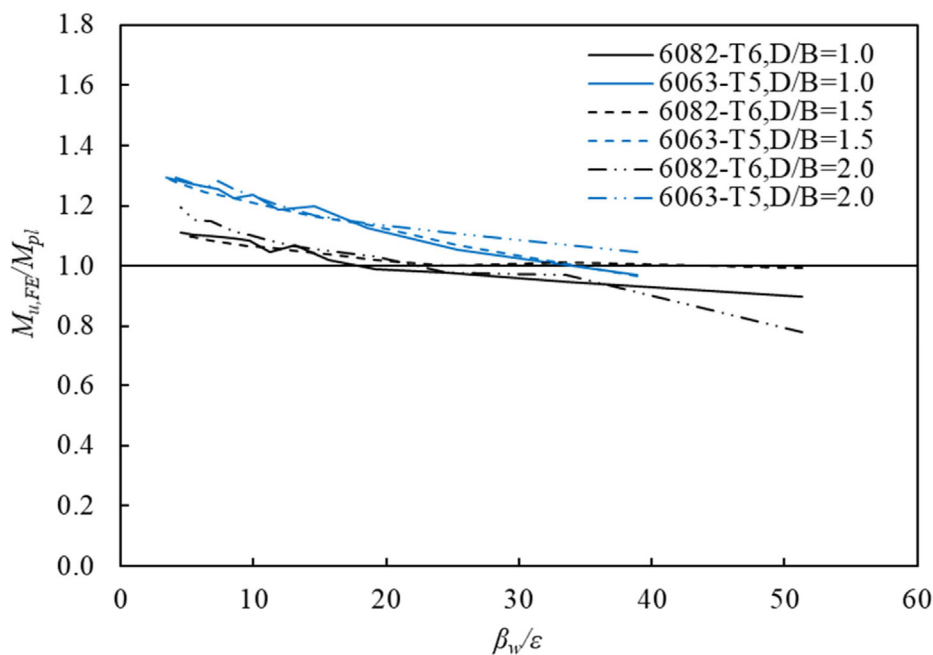


Fig. 12. Normalised bending moment capacity $M_{u,FE} / M_{pl}$ of C-sections under “n” bending orientation.

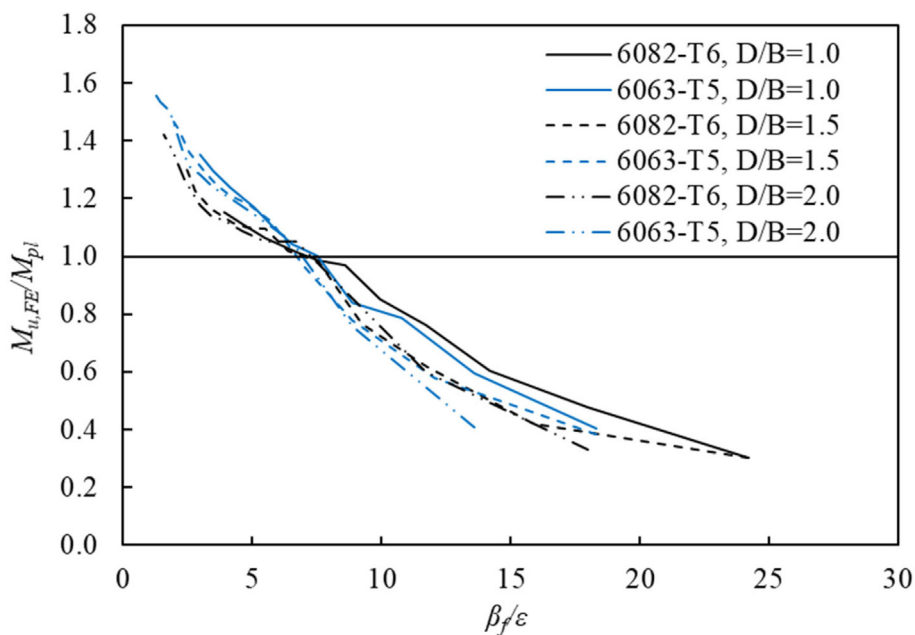


Fig. 13. Normalised bending moment capacity $M_{u,FE} / M_{pl}$ of C-sections under “u” bending orientation.

4.1. EC9

4.1.1. General

EC9 [6] estimates the ultimate bending moment resistance of a cross-section considering the material yield strength and the susceptibility of each constituent plate element to local buckling. Particularly, EC9 [6] classifies the cross-sections in four different classes based on slenderness limits and thus identifies to what extent the cross-sectional flexural resistance is limited by the local buckling resistance. Class 1 or ductile cross-sections are able to develop their plastic moment resistance with sufficient rotational capacity. Class 2 or compact cross-sections are able to develop their plastic moment resistance, whilst their rotational capacity is limited by local buckling. Class 3 or semi-compact

cross-sections are able to develop their elastic moment resistance, although local buckling is liable to prevent reaching their plastic moment resistance. In Class 4 or slender cross-sections, significant local buckling phenomena govern the ultimate behaviour leading to failure prior to the attainment of the proof (yield) strength.

4.1.2. Class 2 and Class 3 slenderness limits for outstand elements under stress gradient

The values of experimental and FE bending moment resistance, M_u , of “u” bending orientation are utilised to assess the EC9 Class 2 and Class 3 slenderness limits for outstand elements under stress gradient. To do so, the M_u values were normalised by the corresponding M_{pl} and M_{el} and were plotted against the slenderness parameter β_f / ϵ of the flange in Figs. 14 and 15, respectively. Fig. 14 will be used for the EC9

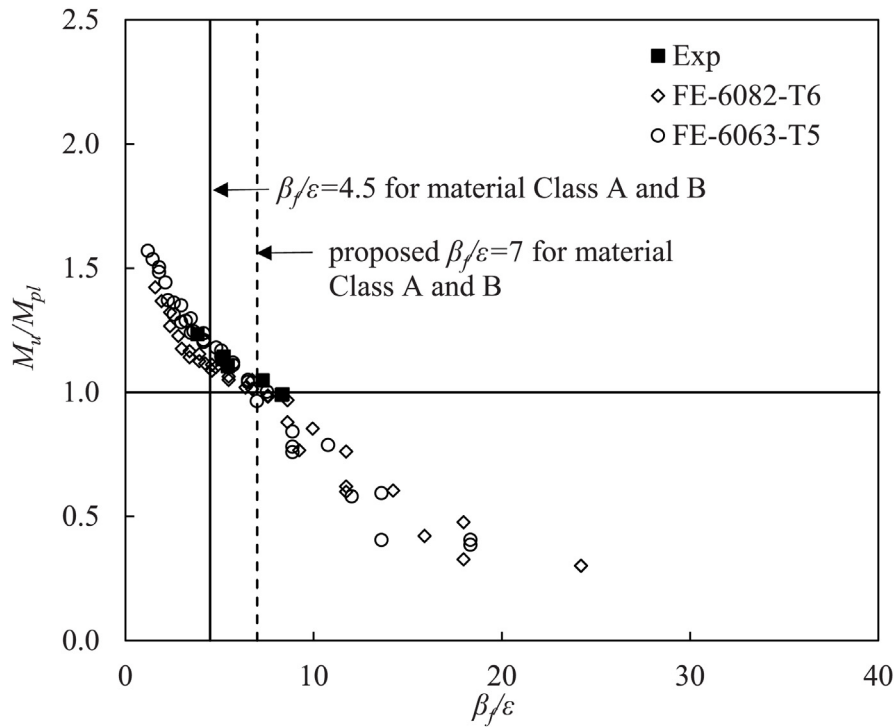


Fig. 14. Assessment of Class 2 slenderness limits for outstand elements under stress gradient.

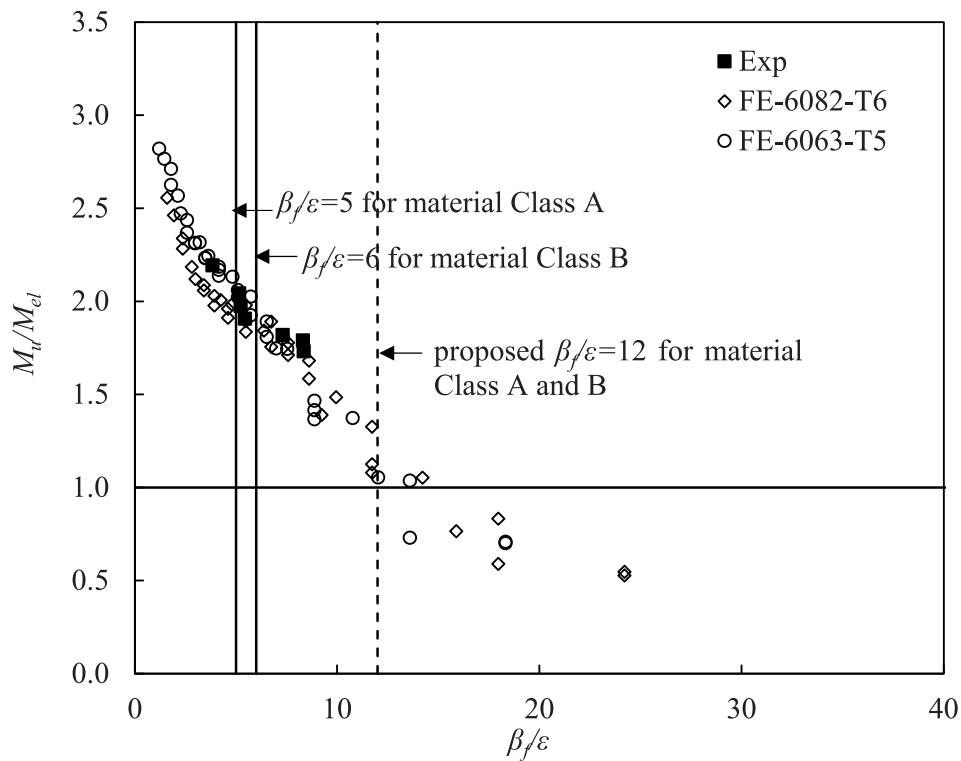


Fig. 15. Assessment of Class 3 slenderness limits for outstand elements under stress gradient.

Class 2 slenderness limits evaluation, whereas Fig. 15 will be used to assess the EC9 Class 3 ones. The Class 2 slenderness limit of $\beta_f/\epsilon = 4.5$ for material Class A and Class B and the Class 3 slenderness limit of $\beta_f/\epsilon = 6$ for material Class A and $\beta_f/\epsilon = 5$ for material Class B are also included in these Figures. For the limits to be accurate, the normalised

moments should be above unity on the left side of the limit and below unity on the right side. As can be seen from both figures, the current slenderness limits are safe but conservative as cross-sections with values of β_f/ϵ ranging from the EC9 limits to 7 and to 12 could reach their plastic and elastic bending moment resistance, respectively. Therefore,

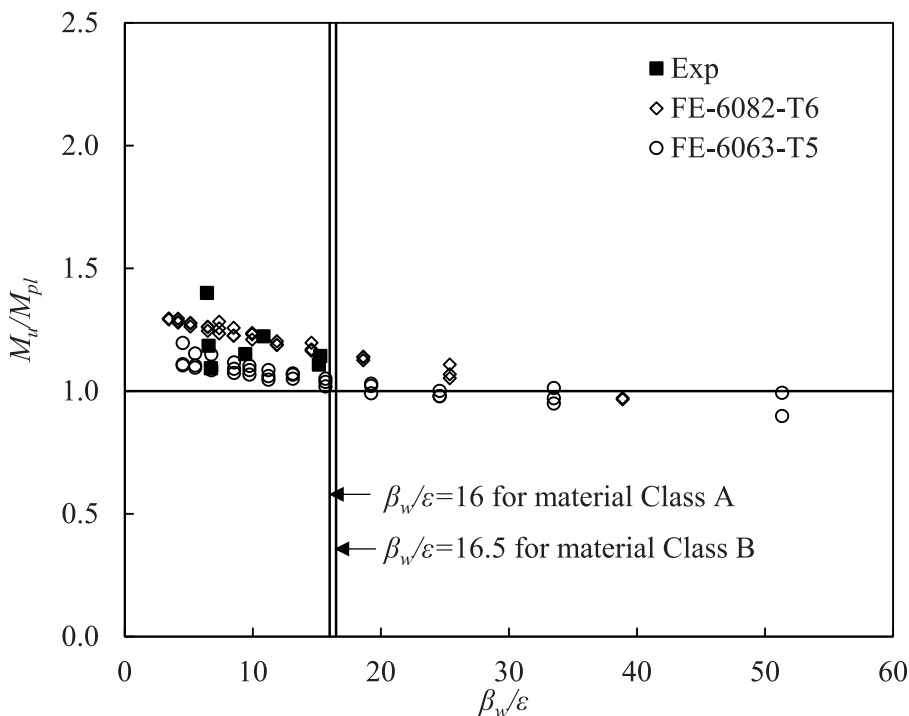


Fig. 16. Assessment of Class 2 slenderness limits for internal elements in compression.

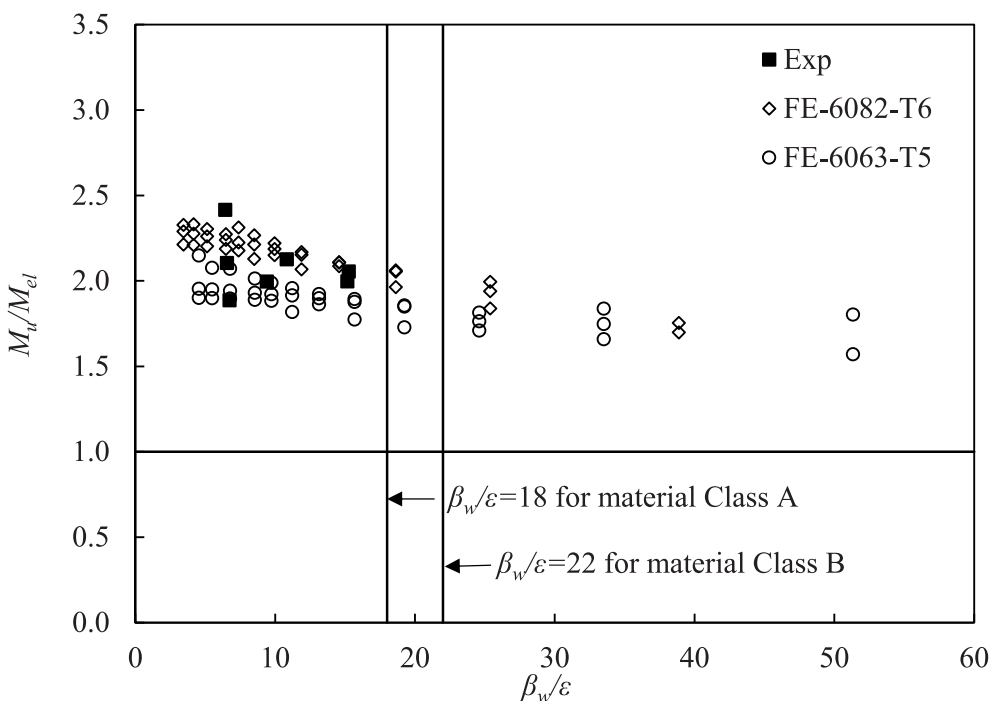


Fig. 17. Assessment of Class 3 slenderness limits for internal elements in compression.

both slenderness limit values could be relaxed leading to more accurate and thereby economical classification results.

4.1.3. Class 2 and Class 3 slenderness limits for internal elements in compression

The obtained data from “n” bending orientation are used to assess the applicability of the EC9 Class 2 and Class 3 slenderness limits for internal elements in compression. The experimental and FE M_u values are normalised by the corresponding M_{pl} and M_{el} and plotted

against the slenderness parameter β_w/ϵ of the web in Figs. 16 and 17, respectively. As can be observed from Fig. 16, the current Class 2 slenderness limits appear accurate, whilst Class 3 limits assessed in Fig. 17 are safe but excessively conservative as all the data points are above and far from the unity threshold line.

4.1.4. Strength predictions

According to Section 6.2.5 specified in EC9 [6], the ultimate bending moment resistance $M_{pred,EC9}$ of C-sections subjected to minor-axis

bending is calculated as follows:

$$M_{pred,EC9} = \alpha_0 W_{el} \sigma_{0.2}, \alpha_0 = \begin{cases} W_{pl}/W_{el} & \text{for Class 1} \\ W_{pl}/W_{el} & \text{for Class 2} \\ 1.0 & \text{for Class 3} \\ W_{eff}/W_{el} & \text{for Class 4} \end{cases} \quad (3)$$

where α_0 is the shape factor, W_{pl} and W_{el} are the plastic and elastic section moduli of the gross cross-section, respectively, and W_{eff} is the effective elastic section modulus of the cross-section calculated using a reduced thickness to consider local buckling effect.

Fig. 18 presents the predicted-to-ultimate $M_{pred,EC9}/M_u$ moment ratios for both bending orientations plotted against the slenderness parameter β_f/ϵ of the flange. The $M_{pred,EC9}/M_u$ ratios are shown separately for the stocky (Classes 1-3) and slender (Class 4) cross-sections. Fig. 18(a) shows that EC9 [6] provides safe and quite accurate design strength predictions for 6082-T6 stocky cross-sections, i.e., $M_{pred,EC9}/M_u$ values close to unity. For the 6063-T5 counterparts, the design strength predictions appear more conservative, since lower $M_{pred,EC9}/M_u$ values are provided, particularly for stockier sections. This is related to the fact that EC9 [6] does not consider the material strain hardening behaviour which is more pronounced for 6063-T5. Conversely, for both 6082-T6 and 6063-T5 slender cross-sections, EC9 [6] underestimates their bending moment capacity, i.e., $M_{pred,EC9}/M_u$ values are much lower than unity. This is related to the overly conservative Class 3 slenderness limit as shown in Fig. 17 that leads to quite underestimated and uneconomical design strength predictions for slender cross-sections. For cross-sections examined with flange tips in compression, i.e., “u” bending orientation, EC9 [6] generally provides quite conservative design strength predictions for both stocky and slender cross-sections as shown in Fig. 18(b). However, for 6082-T6 stocky cross-sections, the predicted bending moment capacities are more accurate than the corresponding ones for 6063-T5 stocky cross-sections owing again to the lack of consideration of the material strain hardening properties.

4.2. Continuous strength method

The CSM is a deformation-based design approach that rationally accounts for the beneficial influence of material strain hardening which allows for stresses higher than the nominal yield strength. The CSM was originally devised for stainless steel and carbon steel cross-sections [46–51], but was also extended to cover aluminium alloy doubly-symmetric cross-sections [52,53]. Recently, the CSM was modified to be applicable on monosymmetric and asymmetric stainless steel cross-sections [20]. The present study assesses the applicability of the design equations proposed by [20] to aluminium alloy C-sections. In non-doubly symmetric cross-sections, the developed stresses at the outer fibres are not equal. The maximum attainable strain in the outer compressive fibre $\epsilon_{CSM,c}$ is obtained from an experimentally derived base curve according to cross-sectional slenderness $\bar{\lambda}_{cs}$ (Eqs. (4)–(6)). The corresponding maximum attainable strain in the outer tensile fibre $\epsilon_{CSM,t}$ is obtained assuming a linearly varying strain distribution through the cross-sectional depth (Eq. (7)). Therefore, the maximum attainable strain of the cross-section ϵ_{CSM} is taken as the maximum absolute value of $\epsilon_{CSM,c}$ and $\epsilon_{CSM,t}$.

$$\frac{\epsilon_{CSM,c}}{\epsilon_{0.2}} = \frac{0.25}{\bar{\lambda}_{cs}^{3.6}} \leq \min(15, \frac{0.5\epsilon_u}{\epsilon_{0.2}}) \quad \text{for } \bar{\lambda}_{cs} \leq 0.68$$

$$\frac{\epsilon_{CSM,c}}{\epsilon_{0.2}} = \left(1 - \frac{0.222}{\bar{\lambda}_{cs}^{1.05}}\right) \frac{1}{\bar{\lambda}_{cs}^{1.05}} \quad \text{for } \bar{\lambda}_{cs} > 0.68 \quad (4)$$

where ϵ_u is the strain at the ultimate tensile stress and $\bar{\lambda}_{cs}$ is the cross-sectional slenderness, given from the Eqs. (5) and (6), respectively.

$$\epsilon_u = 0.13(1 - \frac{\sigma_u}{\sigma_{0.2}}) + 0.059 \quad (5)$$

$$\bar{\lambda}_{cs} = \sqrt{\sigma_{0.2}/\sigma_{cr}} \quad (6)$$

where σ_{cr} is the elastic critical buckling stress of the cross-section considering the element interaction. It can be estimated using either proposed analytical formulae [54] or numerical tools, such as CUFSM [55]. Herein, the analytical formulae available in [54] were utilised to calculate the σ_{cr} . The equation for the calculation of $\epsilon_{CSM,t}$ is the following:

$$\frac{\epsilon_{CSM,t}}{\epsilon_{0.2}} = \frac{\epsilon_{CSM,c}}{\epsilon_{0.2}} \frac{(B - y_c)}{y_c} \quad (7)$$

where B is the cross-sectional width and y_c is the distance from the outer compressive fibre to the neutral axis of the cross-section.

The maximum attainable strain ϵ_{CSM} of the cross-section is given as follows:

$$\frac{\epsilon_{CSM}}{\epsilon_{0.2}} = \max\left(\frac{\epsilon_{CSM,c}}{\epsilon_{0.2}}, \frac{\epsilon_{CSM,t}}{\epsilon_{0.2}}\right) \quad (8)$$

The CSM adopts a bilinear strain hardening material model with a strain hardening modulus, E_{sh} equal to:

$$E_{sh} = \frac{\sigma_u - \sigma_{0.2}}{0.5\epsilon_u - \epsilon_{0.2}} \quad (9)$$

Based on the maximum attainable strain ϵ_{CSM} and the adopted material model, the cross-sectional ultimate moment capacity $M_{pred,CSM}$ is calculated using the following Equation:

$$M_{pred,CSM} = \begin{cases} \frac{\epsilon_{CSM}}{\epsilon_{0.2}} W_{el} \sigma_{0.2} & \text{for } \frac{\epsilon_{CSM}}{\epsilon_{0.2}} < 1.0 \\ W_{pl} \sigma_{0.2} \left[1 + \frac{E_{sh}}{E} \frac{W_{el}}{W_{pl}} \left(\frac{\epsilon_{CSM}}{\epsilon_{0.2}} - 1\right) - \left(1 - \frac{W_{el}}{W_{pl}}\right) / \left(\frac{\epsilon_{CSM}}{\epsilon_{0.2}}\right)^\alpha\right] & \text{for } \frac{\epsilon_{CSM}}{\epsilon_{0.2}} \geq 1.0 \end{cases} \quad (10)$$

where α is a CSM bending coefficient depending on the cross-sectional shape, the axis of bending and the cross-sectional aspect ratio (D/B). Herein, for C-sections bent about the minor axis, α is equal to 1.0 for $D/B > 2$ and 1.5 for $D/B \leq 2$ [20].

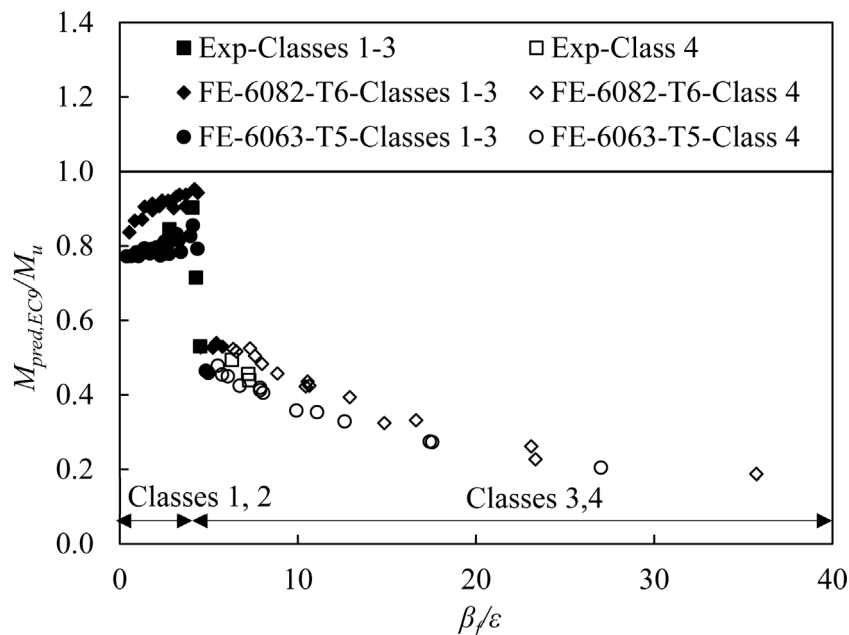
The obtained experimental and FE results were utilised to evaluate the applicability of the CSM for monosymmetric aluminium alloys cross-sections. Fig. 19 depicts the predicted-to-ultimate $M_{pred,CSM}/M_u$ moment ratios for both bending orientations plotted against the cross-sectional slenderness $\bar{\lambda}_{cs}$. The $M_{pred,CSM}/M_u$ ratios are shown separately for the stocky ($\bar{\lambda}_{cs} \leq 0.68$) and slender ($\bar{\lambda}_{cs} > 0.68$) cross-sections. As was expected, the CSM design strength predictions are quite improved compared to the corresponding EC9 ones for the stocky cross-sections under the “n” bending orientation, as they are able to take into account the strain hardening effect. Higher design accuracy is also observed for the cross-sections under the “u” bending orientation and particularly for the slender cross-sections.

4.3. Direct strength method

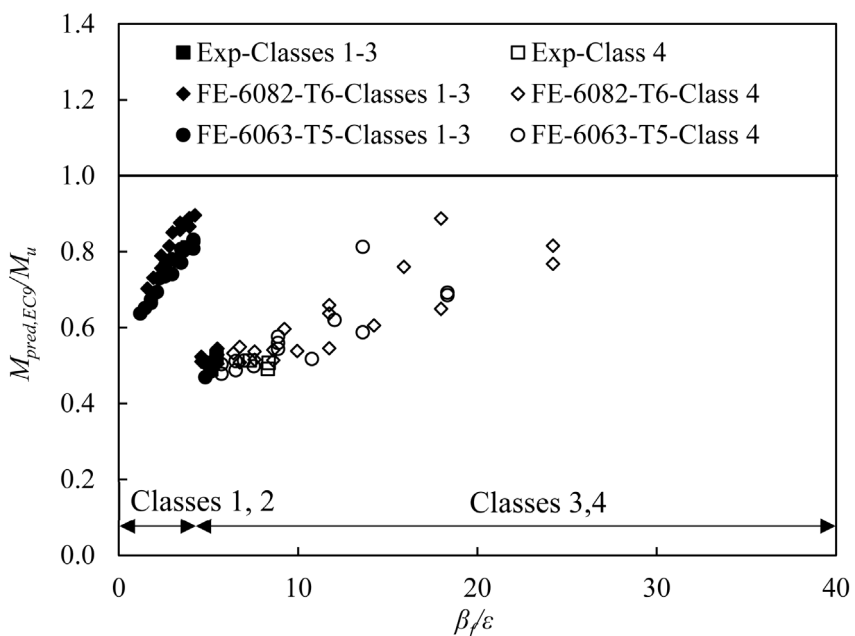
The DSM is codified in Section F3.2.1 of [21] as an alternative and simplified design method compared to the traditional effective width method. The DSM was originally proposed for cold-formed carbon steel members subjected to local or distortional buckling [56,57]. The design formulae account for the beneficial exploitation of the plate element interaction of the considered cross-sections. The cross-sectional flexural strength $M_{pred,DSM}$ is given by Eq. (11) and is equal to the minimum between the local buckling strength M_{nl} and the lateral-torsional buckling strength M_{ne} :

$$M_{pred,DSM} = \min(M_{nl}, M_{ne}),$$

$$M_{nl} = \begin{cases} M_{ne} & \text{for } \bar{\lambda}_{cs} \leq 0.776 \\ \left[1 - 0.15 \left(\frac{M_{crl}}{M_{ne}}\right)^{0.4}\right] \left(\frac{M_{crl}}{M_{ne}}\right)^{0.4} M_{ne} & \text{for } \bar{\lambda}_{cs} > 0.776 \end{cases} \quad (11)$$



(a) “n” bending orientation



(b) “u” bending orientation

Fig. 18. Assessment of EN 1999 – 1 – 1 design strength predictions.

where M_{cr1} is the critical elastic local buckling moment. For C-sections under minor-axis bending, lateral-torsional buckling is excluded and thus M_{ne} is the yield strength.

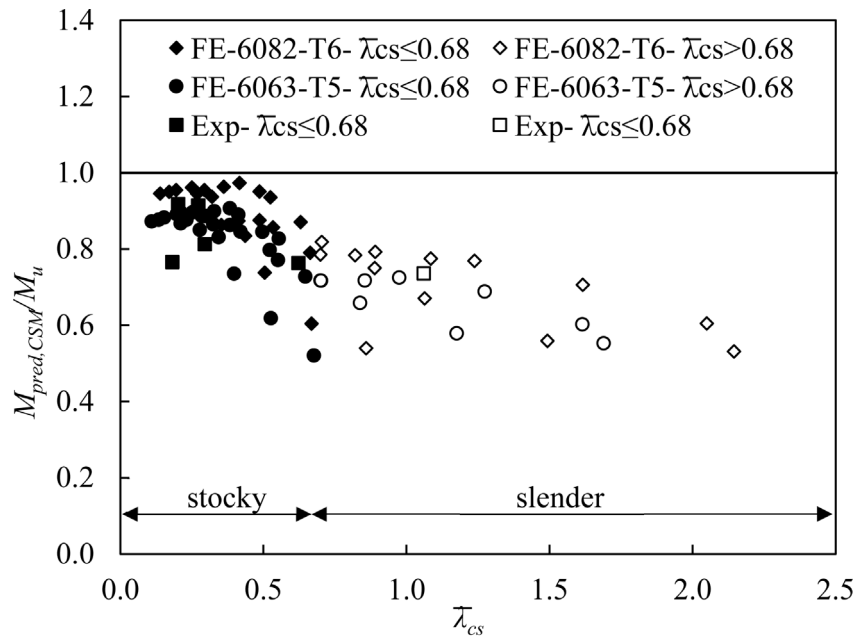
Fig. 20 presents the predicted-to-ultimate $M_{pred,DSM}/M_u$ moment ratios for both bending orientations plotted against the cross-sectional slenderness $\bar{\lambda}_{cs}$. The $M_{pred,DSM}/M_u$ ratios are shown separately for the stocky ($\bar{\lambda}_{cs} \leq 0.776$) and slender ($\bar{\lambda}_{cs} > 0.776$) cross-sections. Fig. 20(a) suggests that the DSM is overly conservative, consistently underestimating the flexural strength of both stocky and slender cross-sections with web in compression, i.e., “n” bending orientation. On the other hand, the DSM design strength predictions for cross-sections with

flange tips in compression, i.e., “u” bending orientation, appear to be more accurate for increasing $\bar{\lambda}_{cs}$, although more scattered (Fig. 20(b)). Moreover, this method assumes that the cross-section exhibits linear stress distribution throughout at failure, which is incorrect as discussed in the following section.

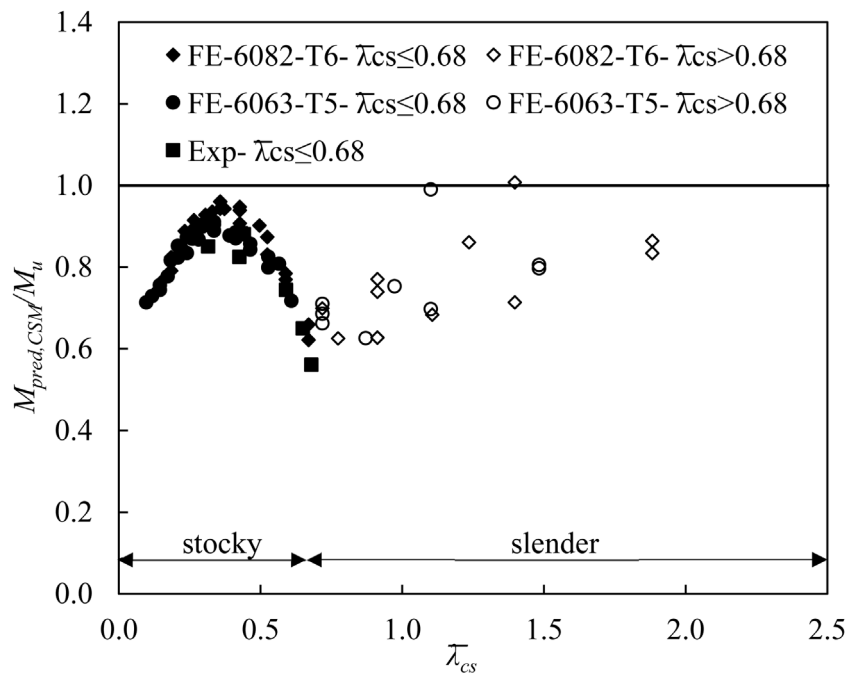
4.4. Plastic effective width method

4.4.1. General

Past studies [30,58,59] on steel slender I-sections subjected to minor axis bending, i.e., having the flange outstands under stress gradient, demonstrated that slender cross-sections often exhibit inelastic



(a) “n” bending orientation

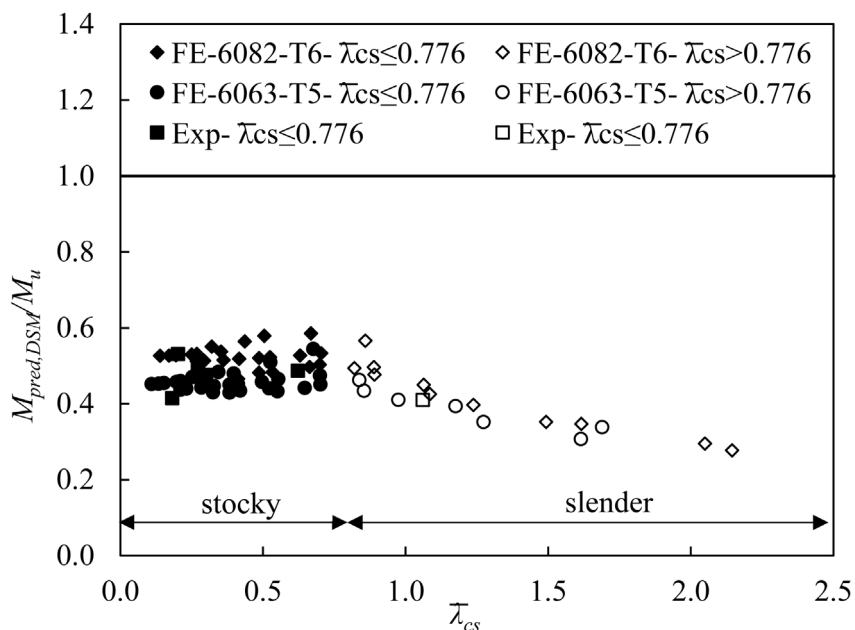


(b) “u” bending orientation

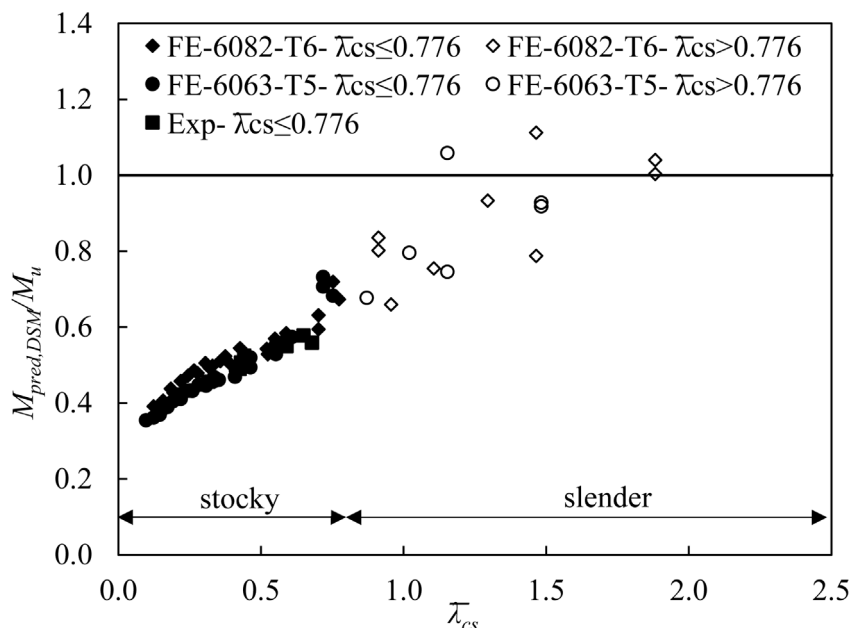
Fig. 19. Assessment of CSM design strength predictions.

response. Particularly, with the onset of local buckling at the compressive flange, the neutral axis shifts towards the cross-sectional part which is initially in tension and usually reaches yielding. Yielding in tension and stress redistribution result in significant post-buckling reserve allowing the cross-section to endure higher loading into the inelastic regime. Moreover, it was found [60] that the strain at the ultimate state can be many times higher than the yield strain. Therefore, the adopted principle of linear elastic stress distribution with the maximum stress at yield capacity is fundamentally incorrect and leads to overly conservative design strength predictions [61]. Bambach

et al. [45] considered these observations to derive a general method, known as plastic effective width method, for strength prediction of slender cross-sections with flange outstands under any stress gradient. This method allows for inelastic strain distribution at the ultimate state assuming that certain parts of the cross-section remain effective, i.e., effective widths, in resisting loading. The proposed plastic effective width formulae and inelastic reserve capacity allowance were validated against test data producing realistic strength predictions for slender cold-formed and hot-rolled I- and C-sections under minor axis bending [61,62].



(a) “n” bending orientation



(b) “u” bending orientation

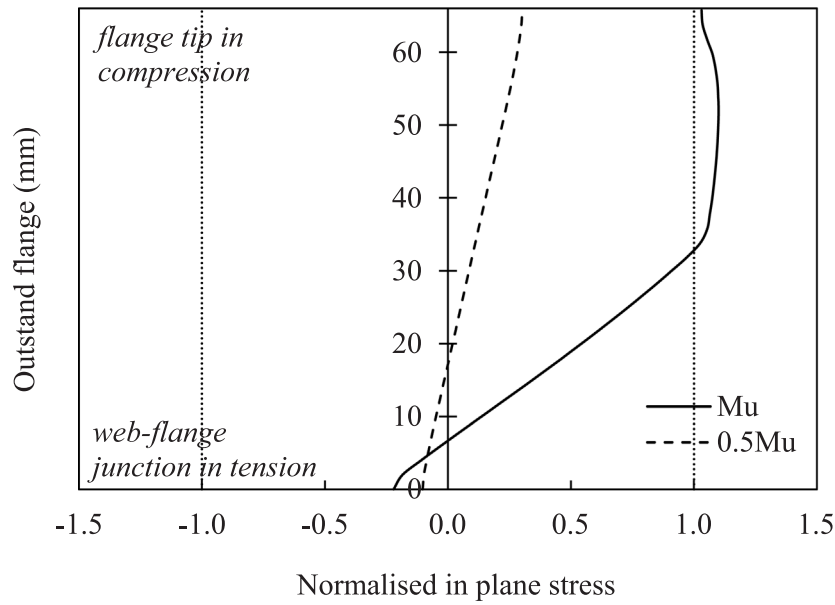
Fig. 20. Assessment of DSM design strength predictions.

The present study investigates whether these observations are also applicable in case of aluminium alloy slender C-sections. On this direction, the stress distribution profiles of the flanges, as obtained from the parametric studies where the full profile could be captured, are evaluated. Figs. 21 and 22 display the in-plane longitudinal stress distribution over the flange at the mid-span of the beam for the slenderest examined cross-sections under “u” and “n” bending orientation, respectively. Particularly, these figures provide the stress distribution in the elastic range when the bending moment of the section is $0.5M_u$ and at failure when M_u is reached. Note that the in-plane stresses are normalised by the corresponding yield stress. Both figures denote that the relative slender C-sections exhibit inelastic reserve capacity which

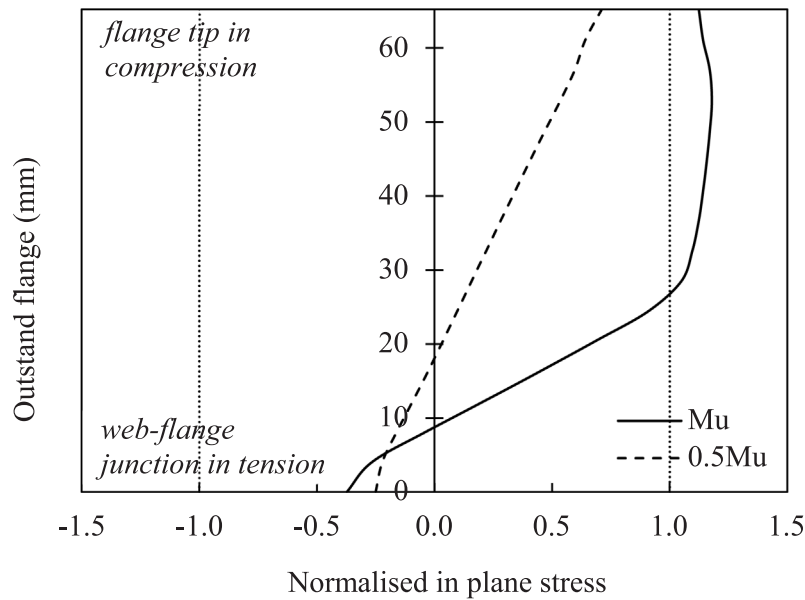
allows for loading higher than the yield strength without failing within the elastic range. This observation is in line with findings for steel C-sections in [30].

4.4.2. Strength predictions – “u” bending orientation

The plastic effective width method suggests that a slender C-section in minor axis bending and under the “u” bending orientation can be designed using a maximum compression strain of C_y times the yield strain ϵ_y , where C_y is given by Eq. (12). Eq. (13) expresses the effective width b_e of the cross-section which resists loading upon local buckling occurrence and is defined at distance e_{cc2} from the flange tip (Eq. (14)).



(a) 6082-T6 ($100 \times 66.7 \times 2 - D/B = 1.5 - \beta_{ff}/\varepsilon = 24.21 - \bar{\lambda}_{cs} = 1.88$)



(b) 6063-T5 ($100 \times 66.7 \times 2 - D/B = 1.5 - \beta_{ff}/\varepsilon = 18.33 - \bar{\lambda}_{cs} = 1.48$)

Fig. 21. Longitudinal stress distribution over the flange at mid-span of the slenderest 6082-T6 and 6063-T5 C-sections under “u” bending configuration.

Following, the distance x_p from the neutral axis of the effective cross-section to the extreme tensile fibre is calculated by Eq. (15). Upon calculation of the parameters defined in Eqs. (16)–(23) and assuming an elastic-perfectly plastic stress distribution, the design flexural strength $M_{pred,pl-ef-f-w}$ can be calculated summing the moments derived from the force resultants of the stress blocks of the effective cross-section. The detailed procedure is given in [45], whilst the involved symbols are explained schematically in Fig. 23.

$$C_y = 3.67 - 1.98 \frac{b_f}{t_f} \sqrt{\frac{\sigma_{0.2}}{E}}, \quad 1 \leq C_y \leq 3 \quad (12)$$

$$b_e = 0.4(1 + \psi) \bar{\lambda}_{cs}^{-0.75} B \leq b_c \quad (13)$$

$$e_{cc2} = 0.55(1 + \psi)B - b_e \quad (14)$$

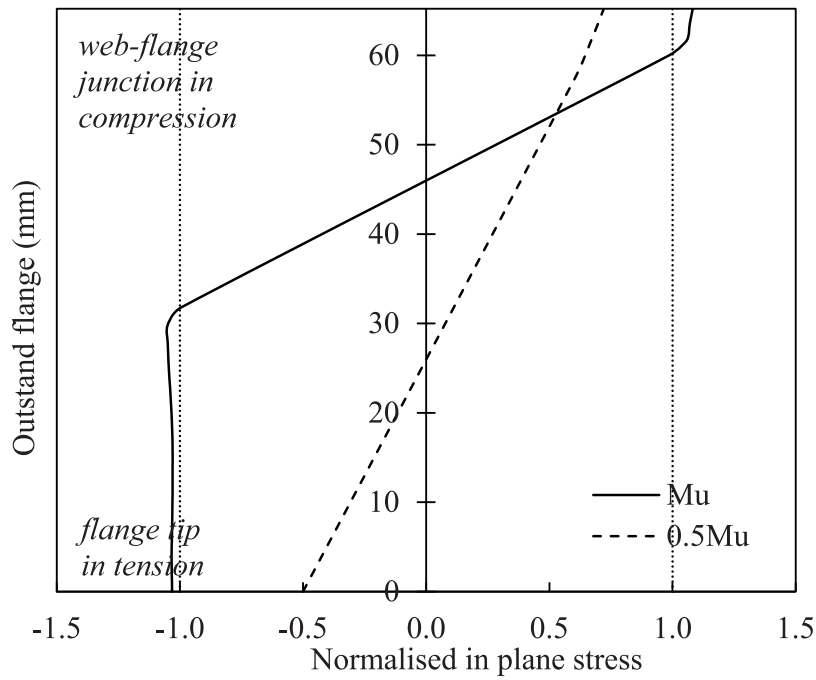
$$x_p = \frac{2b_e t_f (B - b_e/2 - e_{cc2}) + 2b_t t_f b_t/2 + (D - 2t_f) t_w t_w/2}{2b_e t_f + 2b_t t_f + (D - 2t_f) t_w} \quad (15)$$

$$b_t = \frac{B^2 t_f + (D - 2t_f) t_w^2/2}{2B t_f + (D - 2t_f) t_w} \quad (16)$$

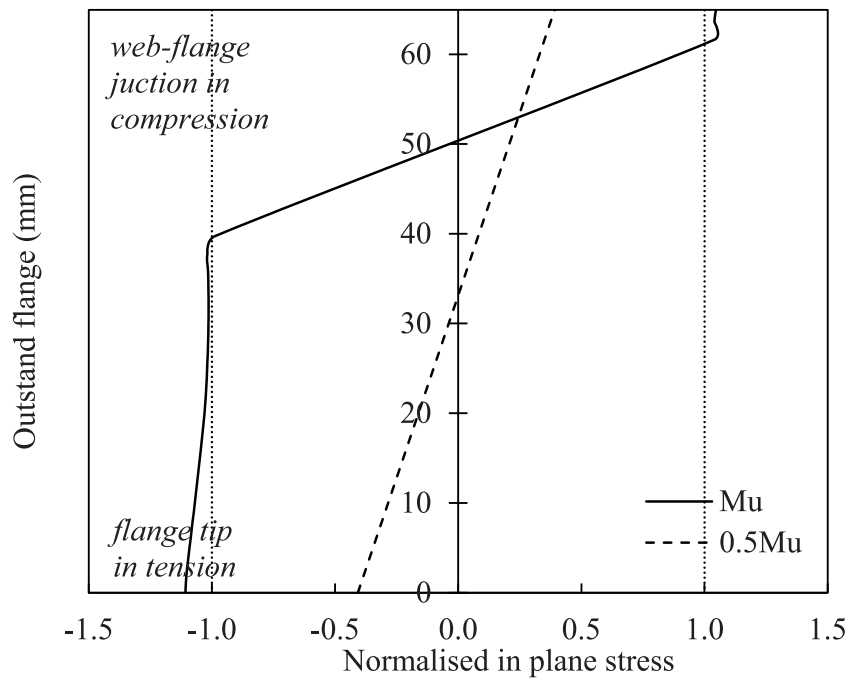
$$K = \frac{C_y \varepsilon_{0.2}}{B - x_p - e_{cc2}} \quad (17)$$

$$b_g = \frac{\varepsilon_{0.2}}{K} \quad (18)$$

$$b_c = B - x_p \quad (19)$$



(a) 6082-T6 ($100 \times 66.7 \times 2$ - $D/B=1.5$ - $\beta_f/\varepsilon=23.33$ - $\bar{\lambda}_{cs}=2.14$)



(b) 6063-T5 ($100 \times 66.7 \times 2$ - $D/B=1.5$ - $\beta_f/\varepsilon=17.55$ - $\bar{\lambda}_{cs}=1.69$)

Fig. 22. Longitudinal stress distribution over the flange at mid-span of the slenderest 6082-T6 and 6063-T5 C-sections under “n” bending configuration.

$$b_p = x_p - 0.5t_w - b_g \tag{20}$$

$$\sigma_w = (x_p - 0.5t_w) KE \tag{21}$$

$$c = b_t - b_g - b_p \tag{22}$$

$$\sigma_c = (cK) E \tag{23}$$

Eqs. (24a) and (24b) are proposed considering the cases of the web being either in elastic or plastic stress state, respectively. If $b_g \geq x_p - 0.5t_w$ the web is under elastic stress state and the design flexural strength $M_{pred,pl-ef-f-w}$ is given by Eq. (24a):

$$M_{pred,pl-ef-f-w} = 2\sigma_{0.2}t_f b_e (B - e_{c2} - b_e/2 - x_p) + \frac{2}{3}\sigma_c t_f c^2 + \frac{2}{3}\sigma_w t_f x_p^2 + \sigma_w t_w (D - 2t_f) (x_p - 0.5t_w) \tag{24a}$$

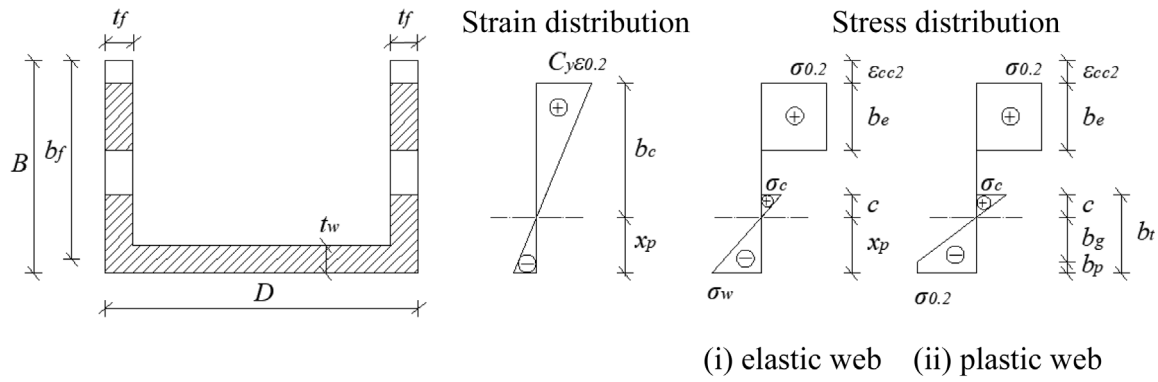


Fig. 23. Plastic Effective Width Method - Strain and stress distribution profiles of the outstand flanges of a C-section under “u” bending orientation.

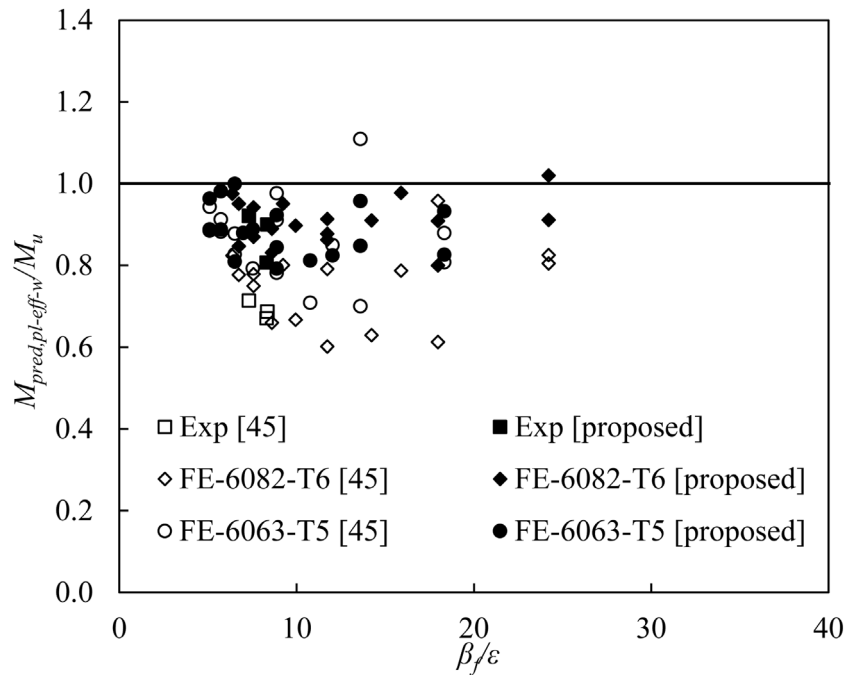


Fig. 24. Assessment of Plastic Effective Width Method design strength predictions for Class 4 C-sections under “u” bending orientation.

If $b_g < x_p - 0.5t_w$ the web is under plastic stress state and the design flexural strength, $M_{pred,pl-eff-w}$, is given by Eq. (24b):

$$M_{pred,pl-eff-w} = 2\sigma_{0.2}t_f b_e (B - e_{cc2} - b_e/2 - x_p) + \frac{2}{3}\sigma_c t_f c^2 + \frac{2}{3}\sigma_{0.2}t_f b_g^2 + 2\sigma_{0.2}t_f b_p (b_g + b_p/2) + \sigma_{0.2}t_w (D - 2t_f) (x_p - 0.5t_w) \quad (24b)$$

To evaluate the applicability of the plastic effective width method on C-sections with tip flanges in compression, the predicted-to-ultimate $M_{pred,pl-eff-w}/M_u$ moment ratios are plotted against the slenderness parameter β_f/ϵ of the flange in Fig. 24. It can be concluded that the design method proposed by [45] provides more accurate strength predictions throughout the considered slenderness range compared to the design codes and methods assessed in Sections 4.1–4.3, but in many cases conservative.

To improve the accuracy and consistency of the plastic effective width method for C-sections, two design equations are proposed to replace Equations (12) and (13) considering the obtained experimental and FE results. The new design proposed equation for the strain coefficient C_y was found using the stress and strain distribution profiles of the C-sections obtained from the parametric studies. As shown in Fig. 23,

C_y is the ratio of the strain at the ultimate state at distance e_{cc2} from the flange tip over the yield strain $\epsilon_{0.2}$. Therefore, the strain coefficient $C_{y,FE}$ was calculated for all the examined C-sections using the corresponding FE in-plane longitudinal strain at the reference location e_{cc2} . According to Fig. 25, the calculated $C_{y,FE}$ values were found to have an exponential relationship with respect to $\frac{b_f}{t_f} \sqrt{\frac{\sigma_{0.2}}{E}}$ which is already used for the calculation of the strain coefficient C_y in Eq. (12). For this reason, regression analysis was conducted for the data of Fig. 25 to obtain Eq. (25) for the calculation of C_y . Aiming to improve the design accuracy and consistency, Eq. (13) for the effective width b_e was recalibrated to Eq. (26) on the basis of the $M_{pred,pl-eff-w}/M_u$ values obtained from the experimental and FE results of this work.

$$C_y = 1.95 \left(\frac{b_f}{t_f} \sqrt{\frac{\sigma_{0.2}}{E}} \right)^{-0.65}, \quad 1 \leq C_y \leq 3 \quad (25)$$

$$b_e = 2.5 \left(\frac{b_f}{t_f} \right)^{-0.8} B \leq b_c \quad (26)$$

The $M_{pred,pl-eff-w}/M_u$ ratios according to the proposed design equations are also plotted in Fig. 24. It can be observed that the use of the plastic effective width method in conjunction with the proposed design equations has significantly improved its accuracy and provides

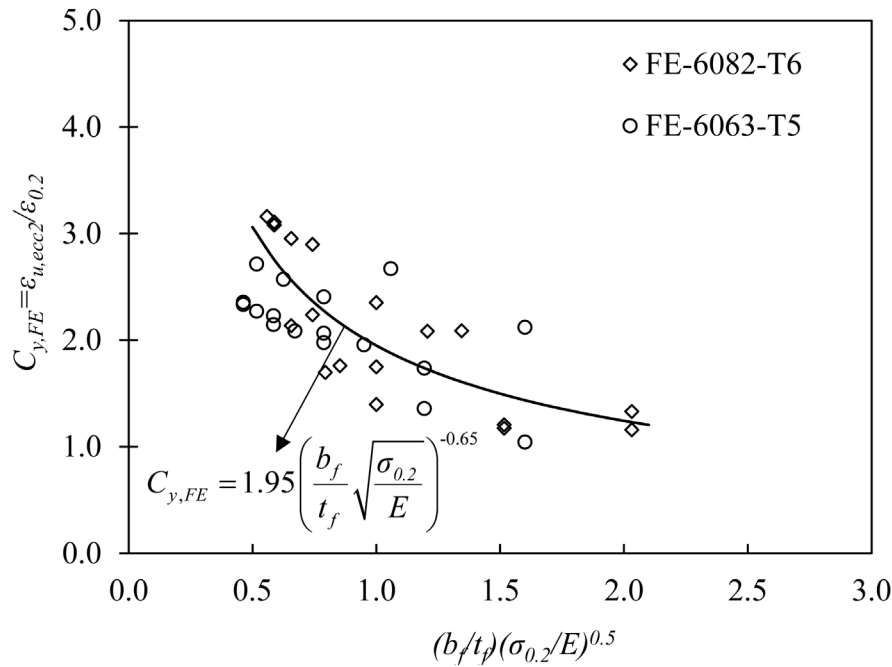


Fig. 25. Strain coefficient $C_{y,FE}$ derived from FE results.

a higher degree of consistency for the bending moment capacities of C-sections with tip flanges in compression.

To further assess the proposed design formulae for the plastic effective width method for C-sections with tip flanges in compression (“u” bending orientation), the stress distribution profiles exported from the FE analyses were compared with the corresponding ones resulted from theoretical calculations. Typical examples of this comparison for both examined aluminium alloys are depicted in Fig. 26 showing a quite good agreement between the numerically and theoretically predicted (using Eqs. (14)–(26)) stress distribution profiles.

4.4.3. Strength predictions - “n” bending orientation

In case of a slender C-section in minor axis bending and under “n” orientation, the maximum compression strain during design can be taken 3 times the yield strain ϵ_y ($C_y = 3$) [45]. For this bending configuration, it was found that for all practical B/t ratios, the compressive strains at the web-flange junction and the tensile strains at the flange tip do not result in lateral displacements in the compressed zone [62]. Thereby, there are no ineffective parts of the cross-section and thus it is assumed that under this strain gradient, the cross-section is fully effective [62]. Similarly to the design procedure of C-sections under the “u” bending orientation and in line with Fig. 27, Eqs. (27)–(31) are used to calculate the basic parameters. The design flexural strength $M_{pred,pl-ef-f-w}$ is determined employing Equation (32).

$$K = \frac{C_y \epsilon_{0.2}}{x_p} \quad (27)$$

$$b_g = \frac{\epsilon_{0.2}}{K} \quad (28)$$

$$b_{pc} = x_p - b_g \quad (29)$$

$$b_t = B - x_p \quad (30)$$

$$b_{pt} = b_t - b_g \quad (31)$$

$$M_{pred,pl-ef-f-w} = \frac{4}{3} \sigma_{0.2} t_f b_g^2 + 2 \sigma_{0.2} t_f b_{pt} (b_g + 0.5 b_{pt}) + 2 \sigma_{0.2} t_f b_{pc} (b_g + 0.5 b_{pc})$$

$$+ \sigma_{0.2} t_w (D - 2t_f) (x_p - 0.5t_w) \quad (32)$$

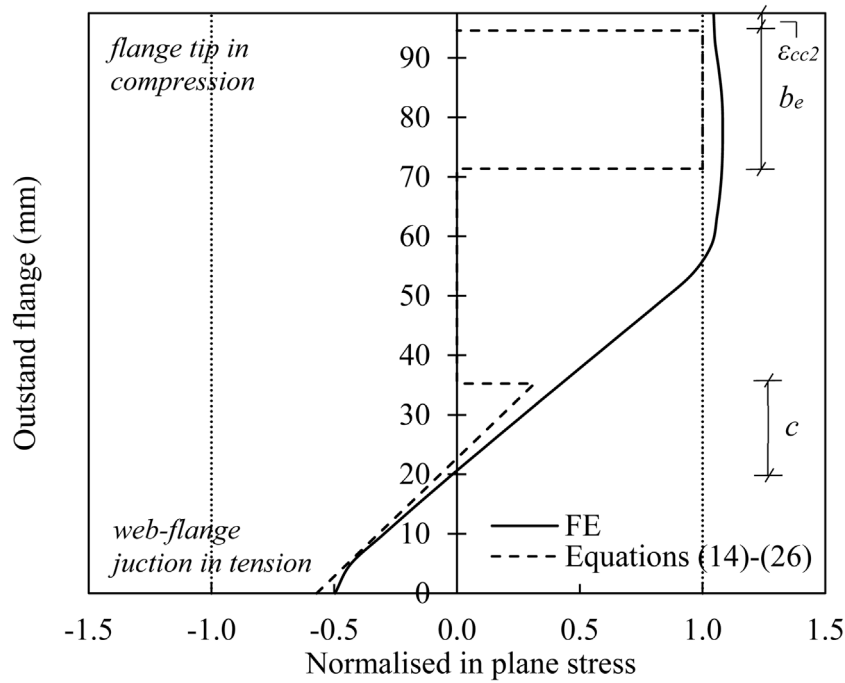
The applicability of the plastic effective width method on C-sections under “n” bending orientation is assessed in Fig. 28, where the predicted-to-ultimate $M_{pred,pl-ef-f-w}/M_u$ moment ratios are plotted against the slenderness parameter β_f/ϵ of the flange. This figure indicates that the design method proposed by [45] generally provides accurate strength predictions for Class 4 6082-T6 and 6063-T5 C-sections under “n” bending orientation.

To further assess the design formulae of the plastic effective width method proposed by [45] for C-sections with web in compression (“n” bending orientation), the stress distribution profiles exported from the FE analyses were compared with the corresponding ones resulted from theoretical calculations. Typical examples of this comparison for both examined aluminium alloys are depicted in Fig. 29 showing a quite good agreement between the numerically and theoretically predicted [45] stress distribution profiles.

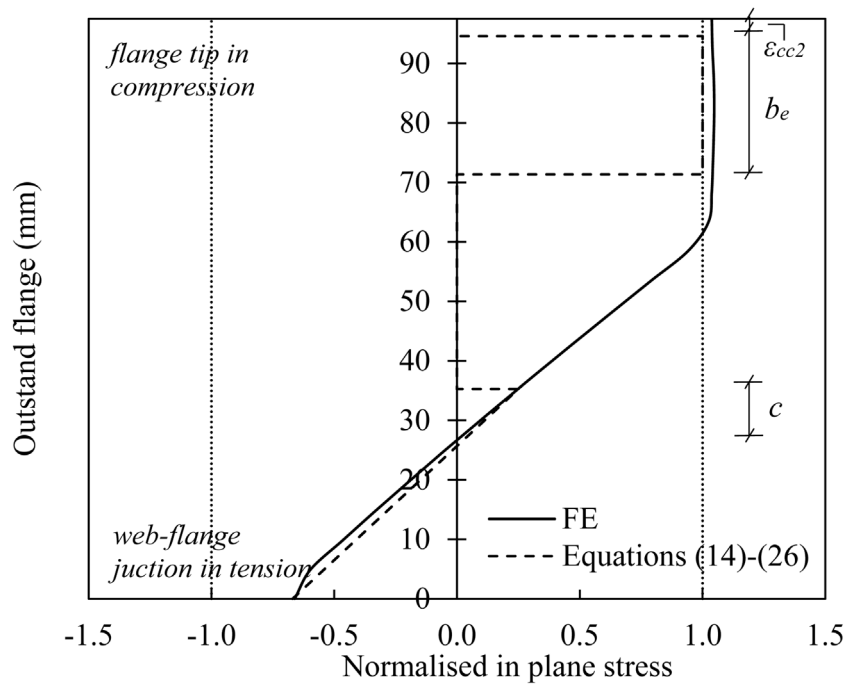
4.5. Comparison of design codes and methods

This section quantifies the design accuracy and consistency provided by the codes and methods previously discussed in Sections 4.1–4.4. For this purpose, the M_{pred}/M_u ratios are summarised in Tables 7 and 8 for the “n” and “u” bending orientation, respectively. The results are also presented separately for stocky and slender cross-sections, where applicable.

Regarding “n” bending orientation, EC9 is conservative for stocky C-sections exhibiting average M_{pred}/M_u ratio of 0.79, whilst for slender C-sections the level of conservatism significantly increases to average M_{pred}/M_u ratio of 0.40. The lack of accuracy is more pronounced for the DSM which consistently underestimates the ultimate bending moment capacities by 53%. Conversely, ultimate bending moment capacities derived from CSM appear to be quite improved for stocky C-sections with average M_{pred}/M_u ratio of 0.85. However, the average M_{pred}/M_u ratio decreases to 0.67 for slender C-sections, showing a significant underestimation of the ultimate bending moment capacities. The plastic effective width method was found to provide accurate and relatively consistent design strength predictions for slender C-sections resulting in average to a M_{pred}/M_u ratio of 0.98 and a corresponding COV value of 0.09.



(a) 6082-T6 ($100 \times 100 \times 5$ - $D/B=1.0$ - $\beta_f/\epsilon=14.23$ - $\bar{\lambda}_{cs}=1.11$)



(b) 6063-T5 ($100 \times 66.7 \times 2$ - $D/B=1.5$ - $\beta_f/\epsilon=10.77$ - $\bar{\lambda}_{cs}=0.87$)

Fig. 26. Comparison between FE and calculated stress distribution for typical 6082-T6 and 6063-T5 C-sections under “u” bending orientation.

Direct comparisons based on the results listed in Table 8 denote that EC9 underestimates by 36% the ultimate bending moment capacities of C-sections under “u” bending orientation. Furthermore, CSM was found to provide the most accurate design strength predictions for stocky C-sections exhibiting an average M_{pred}/M_u ratio of 0.83. On the other hand, the obtained results denote that DSM largely underestimate the ultimate bending moment capacities for stocky C-sections, although it

offers quite accurate design strength predictions for slender C-sections. Improved accuracy and consistency are achieved by the plastic effective width method which results in average to a M_{pred}/M_u ratio of 0.81 and a corresponding COV of 0.13. It was also shown that the proposed design equations are capable of more accurately capturing the plastic stress distribution of the buckled flanges of slender sections increasing the average M_{pred}/M_u ratio to 0.90. Higher design consistency is also

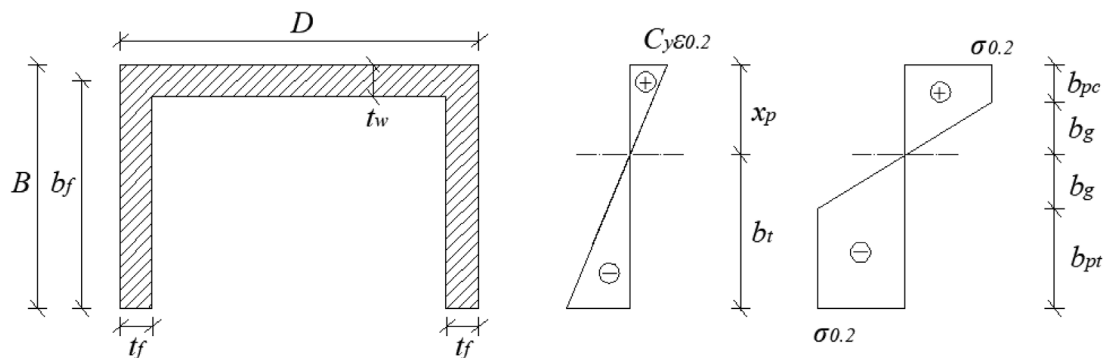


Fig. 27. Plastic Effective Width Method-Strain and stress distribution profiles of the outstand flanges of a C-section under “n” bending orientation.

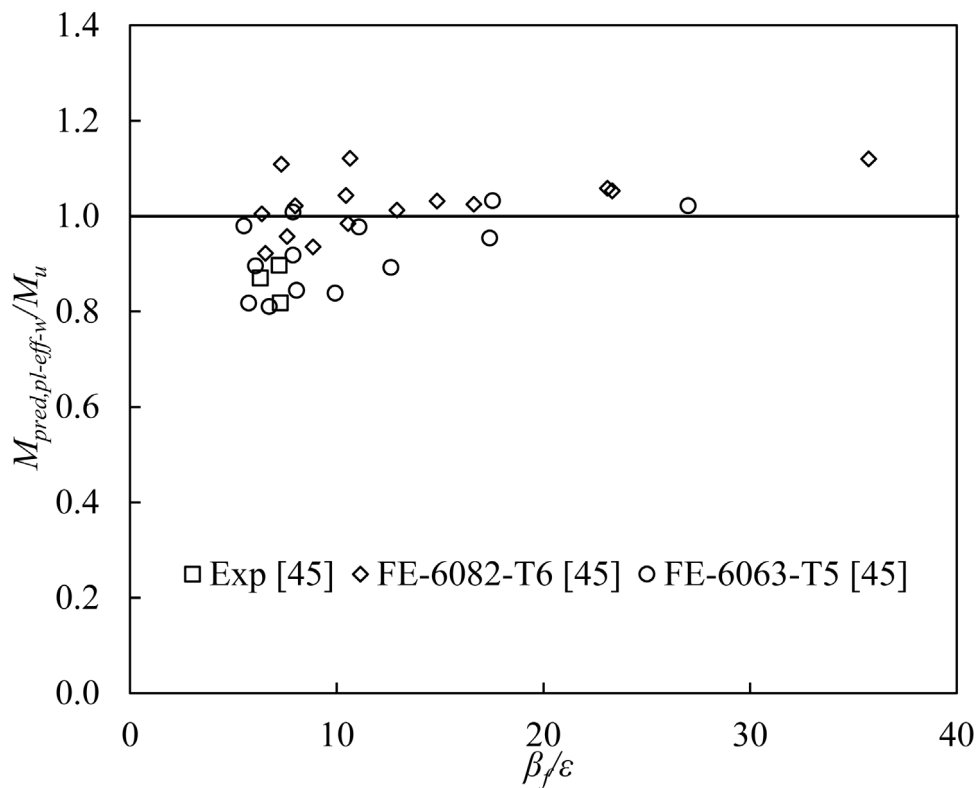


Fig. 28. Assessment of Plastic Effective Width Method design strength predictions for Class 4 C-sections under “n” bending orientation.

achieved since the corresponding COV is further improved to 0.07 which is the lowest value amongst those ones resulted from the codes and the other methods.

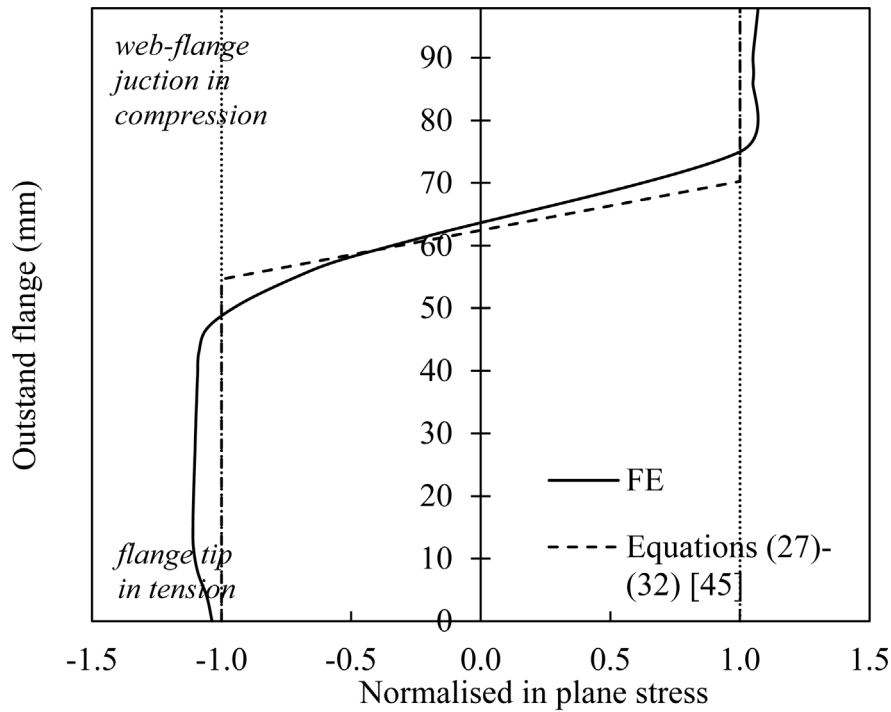
5. Conclusions

The present research study experimentally and numerically investigated the flexural response of C-sections about the minor axis. The following conclusions can be drawn from this research study:

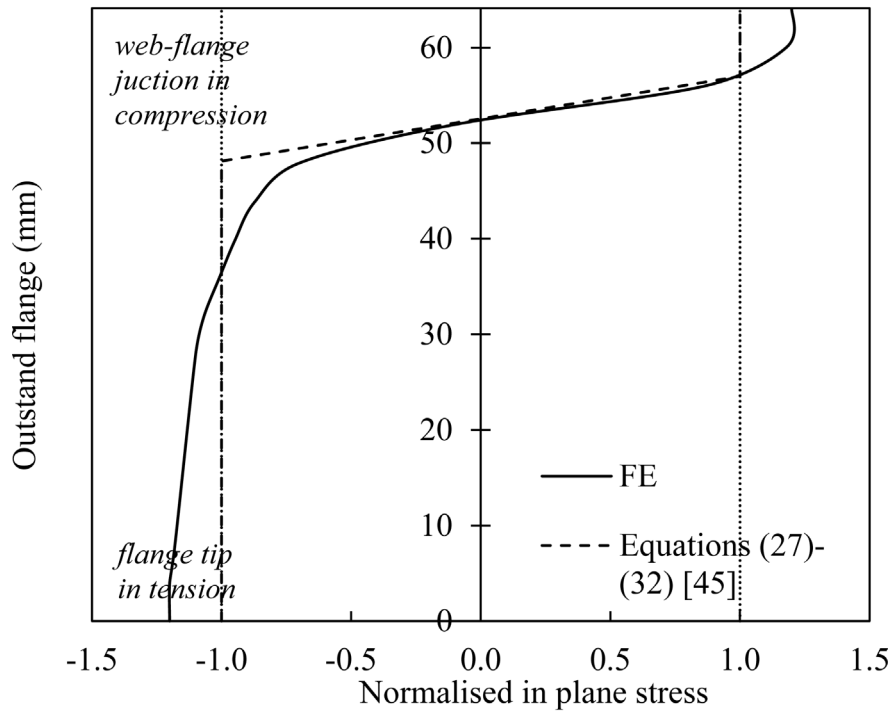
- All beam specimens under “u” bending orientation failed due to local buckling initiated in the compressed part of the flanges. For beam specimens under “n” bending orientation, material yielding was the governing failure mode.
- Assessment of EC9 Class 2 and Class 3 slenderness limits for outstand elements under stress gradient denoted that both values could be relaxed. The same conclusion was drawn for Class 3

slenderness limit for internal elements in compression which was found excessively conservative.

- Regarding C-sections under “n” bending orientation, EC9 provides conservative design strength predictions for stocky cross-sections and the level of conservatism further increases for slender cross-sections. Evaluation of the DSM revealed that it consistently underestimates the ultimate bending moment capacities by 53%. Conversely, CSM appears to offer quite improved results for stocky cross-sections, although it is overly conservative for slender cross-sections.
- Regarding C-sections under “u” bending orientation, EC9 underestimates by 36% the ultimate bending moment capacities. CSM was found to provide the most accurate design strength predictions for stocky cross-sections. DSM is rather conservative for stocky cross-sections, although it offers quite accurate design strength predictions for slender cross-sections.



(a) 6082-T6 ($100 \times 100 \times 4$ - $D/B=1.0$ - $\beta_f/\varepsilon=16.63$ - $\bar{\lambda}_{cs}=1.40$)



(b) 6063-T5 ($100 \times 66.7 \times 4$ - $D/B=1.5$ - $\beta_f/\varepsilon=7.89$ - $\bar{\lambda}_{cs}=0.72$)

Fig. 29. Comparison between FE and calculated stress distribution for typical 6082-T6 and 6063-T5 C-sections under “n” bending orientation.

• The applicability of the plastic effective width method to aluminium alloy C-sections was evaluated, leading to quite accurate and consistent design strength predictions. Modified design

equations were proposed for “u” bending orientation which further improved the accuracy and consistency of the original design formulae by 11% and 50%, respectively. Overall, it is

Table 7
Assessment of design strength predictions for C-sections under “n” bending orientation.

	M_{pred}/M_u											
	6082-T6 (Exp)			6082-T6 (FE)			6063-T5 (FE)			All		
	No Exp	mean	COV	No FE	mean	COV	No FE	mean	COV	No (Exp + FE)	mean	COV
Stocky cross-sections												
EC9 (Classes 1-3)	4	0.75	0.19	20	0.82	0.18	22	0.77	0.13	46	0.79	0.17
CSM ($\lambda_{cs} \leq 0.68$)	6	0.84	0.08	21	0.89	0.10	21	0.83	0.11	48	0.85	0.11
DSM ($\lambda_{cs} \leq 0.776$)	6	0.48	0.07	23	0.52	0.06	27	0.46	0.05	56	0.49	0.08
Slender cross-sections												
EC9 (Class 4)	3	0.46	0.05	15	0.40	0.27	13	0.37	0.21	31	0.40	0.24
CSM ($\lambda_{cs} > 0.68$)	1	0.74	0.00	14	0.68	0.15	14	0.64	0.13	29	0.67	0.14
DSM ($\lambda_{cs} > 0.776$)	1	0.41	0.00	12	0.42	0.20	8	0.40	0.15	21	0.41	0.18
Plastic effective width [45] (Class 4)	3	0.86	0.04	15	1.03	0.06	13	0.93	0.09	31	0.98	0.09
All cross-sections												
EC9 (All)	7	0.63	0.28	35	0.64	0.39	35	0.62	0.34	77	0.63	0.36
CSM (All)	7	0.83	0.09	35	0.81	0.17	35	0.78	0.15	77	0.80	0.16
DSM (All)	7	0.47	0.09	35	0.49	0.15	35	0.44	0.10	77	0.47	0.13

Table 8
Assessment of design strength predictions for C-sections under “u” bending orientation.

	M_{pred}/M_u											
	6082-T6 (Exp)			6082-T6 (FE)			6063-T5 (FE)			All		
	No Exp	mean	COV	No FE	mean	COV	No FE	mean	COV	No (Exp + FE)	mean	COV
Stocky cross-sections												
EC9 (Classes 1-3)	4	0.58	0.23	17	0.71	0.21	18	0.73	0.12	39	0.71	0.19
CSM ($\lambda_{cs} \leq 0.68$)	7	0.77	0.15	22	0.86	0.11	26	0.83	0.07	55	0.83	0.10
DSM ($\lambda_{cs} \leq 0.776$)	7	0.52	0.08	26	0.52	0.14	29	0.48	0.20	62	0.50	0.17
Slender cross-sections												
EC9 (Class 4)	3	0.50	0.02	18	0.62	0.18	17	0.56	0.16	38	0.59	0.18
CSM ($\lambda_{cs} > 0.68$)	–	–	–	13	0.77	0.14	9	0.75	0.14	22	0.76	0.14
DSM ($\lambda_{cs} > 0.776$)	–	–	–	9	0.89	0.16	6	0.87	0.15	15	0.88	0.16
Plastic effective width [45] (Class 4)	3	0.69	0.03	18	0.78	0.12	17	0.88	0.10	38	0.81	0.13
Proposed design method (Class 4)	3	0.88	0.06	18	0.91	0.06	17	0.89	0.07	38	0.90	0.07
All cross-sections												
EC9 (All)	7	0.55	0.20	35	0.67	0.21	35	0.65	0.19	77	0.64	0.19
CSM (All)	7	0.77	0.15	35	0.83	0.13	35	0.81	0.10	77	0.81	0.12
DSM (All)	7	0.52	0.08	35	0.61	0.31	35	0.55	0.33	77	0.58	0.31

recommended that the plastic effective width method can be employed for the design of slender aluminium alloy C-sections subjected to minor axis bending.

CRediT authorship contribution statement

Evangelia Georgantzia: Conceptualization, Data curation, Formal analysis, Investigation, Validation, Software, Methodology, Visualization, Writing – original draft. **Michaela Gkantou:** Conceptualization, Funding acquisition, Methodology, Supervision, Visualization, Writing – review & editing. **George S. Kamaris:** Funding acquisition, Writing – review & editing, Supervision. **Kunal D. Kansara:** Supervision, Writing – review & editing.

Declaration of competing interest

The authors declare that they have no known competing financial interests or personal relationships that could have appeared to influence the work reported in this paper.

Acknowledgements

The authors are grateful to the technicians of the Schools of Civil Engineering and Built Environment and the School of Engineering at Liverpool John Moores University for their valuable assistance. The financial support of the Faculty of Engineering and Technology of Liverpool John Moores University, United Kingdom is also gratefully acknowledged.

References

- [1] E. Georgantzia, M. Gkantou, G.S. Kamaris, Aluminium alloys as structural material : A review of research, *Eng. Struct.* 227 (2021) 111372.
- [2] B.S. Opheim, Bending of Thin-Walled Aluminium Extrusions, Norwegian University of Science and Technology, 1996.
- [3] L.A. Moen, O.S. Hopperstad, M. Langseth, Rotational capacity of aluminum beams under moment gradient. I: Experiments, *J. Struct. Eng.* 125 (8) (1999) 910–920.
- [4] L.A. Moen, G. De Matteis, O.S. Hopperstad, M. Langseth, R. Landolfo, Rotational capacity of aluminum beams under moment gradient. II: Numerical simulations, *J. Struct. Eng.* 125 (8) (1999) 921–929.
- [5] G. De Matteis, L.A. Moen, M. Langseth, R. Landolfo, O.S. Hopperstad, F.M. Mazzolani, Cross-sectional classification for aluminum beams-parametric study, *J. Struct. Eng.* 127 (3) (2001) 271–279.
- [6] European Committee for Standardization (EC9), Eurocode 9 : Design of Aluminium Structures. Part 1-1: General Structural Rules - General Structural Rules and Rules for Buildings, BS EN 1999-1-1:2007, CEN:2007. BSI, 2007.
- [7] M.-N. Su, B. Young, L. Gardner, Deformation-based design of aluminium alloy beams, *Eng. Struct.* 80 (2014) 339–349.
- [8] M.-N. Su, B. Young, L. Gardner, Continuous beams of aluminum alloy tubular cross sections, I: tests and FE model validation, *J. Struct. Eng.* 141 (9) (2015).
- [9] M.-N. Su, B. Young, L. Gardner, Continuous beams of aluminum alloy tubular cross sections, II: parametric study and design, *J. Struct. Eng.* 141 (9) (2015).
- [10] M.-N. Su, B. Young, L. Gardner, Flexural response of aluminium alloy SHS and RHS with internal stiffeners, *Eng. Struct.* 121 (2016) 170–180.
- [11] J.-H. Zhu, B. Young, Design of aluminum alloy flexural members using direct strength method, *J. Struct. Eng.* 135 (5) (2009) 558–566.
- [12] Y. Kim, T. Peköz, Ultimate flexural strength of aluminum sections, *Thin-Walled Struct.* 48 (2010) 857–865.
- [13] P. Castaldo, E. Nastro, V. Piluso, Ultimate behaviour of RHS temper T6 aluminium alloy beams subjected to non-uniform bending: Parametric analysis, *Thin-Walled Struct.* 115 (2017) 129–141.

- [14] V. Piluso, A. Pisapia, E. Nastro, R. Montuori, Ultimate resistance and rotation capacity of low yielding high hardening aluminium alloy beams under non-uniform bending, *Thin-Walled Struct.* 135 (2019) 123–136.
- [15] Y. Zhao, X. Zhai, Bending strength and design methods of the 6082-T6 aluminum alloy beams with circular hollow sections, *Structures* 26 (2020) 870–887.
- [16] R. Feng, Z. Chen, C. Shen, K. Roy, B. Chen, J.B.P. Lim, Flexural capacity of perforated aluminium CHS tubes – an experimental study, *Structures* 25 (2020) 463–480.
- [17] R. Feng, C. Shen, J. Lin, Finite-element analysis and design of aluminium alloy CHSs with circular through-holes in bending, *Thin-Walled Struct.* 144 (2019) 106289.
- [18] J. Zhu, Z. Li, M. Su, B. Young, Design of aluminum alloy channel section beams, *J. Struct. Eng.* 146 (5) (2020) 04020074.
- [19] N.H. Pham, C.H. Pham, K.J.R. Rasmussen, Global buckling capacity of cold-rolled aluminium alloy channel section beams, *J. Constr. Steel Res.* 179 (2021) 106521.
- [20] O. Zhao, L. Gardner, The continuous strength method for the design of mono-symmetric and asymmetric stainless steel cross-sections in bending, *J. Constr. Steel Res.* 150 (2018) 141–152.
- [21] North American Specification for the Design of Cold-Formed Steel Structural Members, American Iron and Steel Institute, Washington, DC, 2012, (AISI S100-12).
- [22] European Committee for Standardization (CEN), Metallic materials – tensile testing – Part 1: Method of test at room temperature. Brussels, 2009.
- [23] W. Ramberg, W.R. Osgood, Description of Stress–Strain Curves By Three Parameters. Technical, National Advisory Committee for Aeronautics, Washington, D.C., 1943.
- [24] H.N. Hill, J.W. Clark, R.J. Brungraber, Design of welded aluminum structures, *J. Struct. Div. ASCE* 86 (6) (1960) 101–124.
- [25] M. Theofanous, A. Liew, L. Gardner, Experimental study of stainless steel angles and channels in bending, *Structures* 4 (2015) 80–90.
- [26] L. Zhang, F. Wang, Y. Liang, O. Zhao, Experimental and numerical studies of press-braked S690 high strength steel channel section beams, *Thin-Walled Struct.* 148 (2020) 106499.
- [27] T.M. Chan, Gardner L bending strength of hot-rolled elliptical hollow sections, *J. Constr. Steel Res.* 64 (2008) 971–986.
- [28] L. Zhang, F. Wang, Y. Liang, O. Zhao, Press-braked S690 high strength steel equal-leg angle and plain channel section stub columns: Testing, numerical simulation and design, *Eng. Struct.* 201 (2019) 109764.
- [29] Karlsson Sorensen Hibbit, ABAQUS: Theory Manual, Dassault Systemes Corporation, Providence, RI, USA, 2018.
- [30] M. Gkantou, M. Bock, M. Theofanous, Design of stainless steel cross-sections with outstand elements under stress gradients, *J. Constr. Steel Res.* 179 (2021) 106491.
- [31] E. Georgantzia, M. Gkantou, G.S. Kamaris, K. Kansara, K. Hashim, Aluminium alloy cross-sections under uniaxial bending and compression : A numerical study, *IOP Conf. Ser. Mater. Sci. Eng.* 1058 (2021) 012011.
- [32] E. Georgantzia, M. Gkantou, G.S. Kamaris, Numerical modelling and design of aluminium alloy angles under uniform compression, *Civ. Eng.* 2 (3) (2021) 632–651.
- [33] S. Bin Ali, E. Georgantzia, M. Gkantou, G.S. Kamaris, P. Kot, Experimental study of square and rectangular hollow section aluminium alloy columns, in: 15th Global Congress on Manufacturing and Management, GCMM2020, Liverpool, England, 2020.
- [34] M. Gkantou, N. Antoniou, M. Theofanous, C. Baniotopoulos, Compressive behaviour of high-strength steel cross-sections, *Struct. Build.* 170 (2017) 1–12.
- [35] M. Gkantou, G. Kokosis, M. Theofanous, S. Dirar, Plastic design of stainless steel continuous beams, *J. Constr. Steel Res.* 152 (2019) 68–80.
- [36] M. Gkantou, M. Theofanous, C. Baniotopoulos, Plastic design of hot-finished high strength steel continuous beams, *Thin-Walled Struct.* 133 (2018) 85–95.
- [37] M. Theofanous, N. Saliba, O. Zhao, L. Gardner, Ultimate response of stainless steel continuous beams, *Thin-Walled Struct.* 83 (2014) 115–127.
- [38] F. Zhou, B. Young, Aluminum tubular sections subjected to web crippling-Part I: Tests and finite element analysis, *Thin-Walled Struct.* 46 (4) (2008) 339–351.
- [39] J.-H. Zhu, B. Young, Numerical investigation and design of aluminum alloy circular hollow section columns, *Thin-Walled Struct.* 46 (2008) 1437–1449.
- [40] K.J.R. Rasmussen, G.J. Hancock, Design of thin-walled plain channel section columns against flexural buckling, *Thin-Walled Struct.* 20 (1–4) (1994) 219–240.
- [41] M. Jandera, L. Gardner, J. Machacek, Residual Stresses in Cold-Rolled Stainless Steel Hollow Sections, Vol. 64, 2008, pp. 1255–1263.
- [42] F.M. Mazzolani, Aluminum Alloy Structures, second ed., E & FN Spon, London, 1995.
- [43] R. Feng, J. Liu, Numerical investigation and design of perforated aluminium alloy SHS and RHS columns, *Eng. Struct.* (2019) 199.
- [44] F. Wang, B. Young, L. Gardner, Compressive testing and numerical modelling of concrete-filled double skin CHS with austenitic stainless steel outer tubes, *Thin Walled Struct.* 141 (2019) 345–359.
- [45] M.R. Bambach, K.J.R. Rasmussen, V. Ungureanu, Inelastic behaviour and design of slender I-sections in minor axis bending, *J. Constr. Steel Res.* 63 (1) (2007) 1–12.
- [46] L. Gardner, F. Wang, A. Liew, Influence of strain hardening on the behavior and design of steel structures, *Int. J. Struct. Stab. Dyn.* 11 (5) (2011) 855–875.
- [47] L. Gardner, M. Ashraf, Structural design for non-linear metallic materials, *Eng. Struct.* 28 (6) (2006) 926–934.
- [48] L. Gardner, The continuous strength method, *Struct. Build.* 161 (SB3) (2008) 127–133.
- [49] L. Gardner, M. Theofanous, Discrete and Continuous Treatment of Local Buckling in Stainless Steel Elements, Vol. 64, 2008, pp. 1207–1216.
- [50] S. Afshan, L. Gardner, The continuous strength method for structural stainless steel design, *Thin Walled Struct.* 68 (2013) 42–49.
- [51] O. Zhao, S. Afshan, L. Gardner, Structural response and continuous strength method design of slender stainless steel cross-sections, *Eng. Struct.* 140 (2017) 14–25.
- [52] M.-N. Su, B. Young, L. Gardner, The continuous strength method for the design of aluminium alloy structural elements, *Eng. Struct.* 122 (2016) 338–348.
- [53] M.-N. Su, B. Young, L. Gardner, Testing and design of aluminum alloy cross sections in compression, *J. Struct. Eng.* 140 (9) (2014) 04014047.
- [54] M. Seif, B.W. Schafer, Local buckling of structural steel shapes, *J. Constr. Steel Res.* 66 (10) (2010) 1232–1247.
- [55] Z. Li, B.W. Schafer, Buckling analysis of cold-formed steel members with general boundary conditions using CUFISM: conventional and constrained finite strip methods, in: 20th International Specialty Conference on Cold-Formed Steel Structures. St. Louis, Missouri, U.S.A., 2010.
- [56] B.W. Schafer, T. Peköz, Direct strength prediction of cold-formed steel members using numerical elastic buckling solutions, in: *Int Spec Conf Cold-Formed Steel Struct Recent Res Dev Cold-Formed Steel Des Constr*, 1998, pp. 69–76.
- [57] B.W. Schafer, Review: The direct strength method of cold-formed steel member design, *J. Constr. Steel Res.* 64 (7–8) (2008) 766–778.
- [58] G.C. Chick, Thin Walled I-Sections in Compression and Bending (Ph.D. thesis), Dept. of Civil Engineering, Univ. of Sydney, Sydney, Australia.
- [59] A. Rusch, J. Lindner, Remarks to the direct strength method, *Thin-Walled Struct.* 39 (2001) 807–820.
- [60] M.R. Bambach, K.J.R. Rasmussen, Tests of Unstiffened Plate Elements Under Combined Compression and Bending, Vol. 130, 2004, pp. 1602–1610.
- [61] M.R. Bambach, K.J.R. Rasmussen, Design Provisions for Sections Containing Unstiffened Elements with Stress Gradient, Vol. 130, 2004, pp. 1620–1628.
- [62] M.R. Bambach, K.J.R. Rasmussen, Effective Widths of Unstiffened Elements with Stress Gradient, Vol. 130. No. 10, 2006, pp. 1611–1619.